INTERACTION OF THE GEOMAGNETIC FIELD WITH NORTHWARD

INTERPLANETARY MAGNETIC FIELD

by

SHREE KRISHNA BHATTARAI

Presented to the Faculty of the Graduate School of

The University of Texas at Arlington in Partial Fulfillment

of the Requirements

for the Degree of

DOCTOR OF PHILOSOPHY

THE UNIVERSITY OF TEXAS AT ARLINGTON

May 2013

To my parents who were the first teacher of my life

ACKNOWLEDGEMENTS

Finally, I would like to express my deep gratitude to my parents, who have encouraged, inspired, and financed me to continue my education, even during times of hardship. I would like to acknowledge my deceased father, who taught me how to handle the tools related to the greatest scientific research - life. Thanks to my wife for standing by my side all this time, for her sacrifice and patience and helping me keep high morale. Thanks to my cute son, for being one more reason I want to be a better person in my life.

April 12, 2013

ABSTRACT

INTERACTION OF THE GEOMAGNETIC FIELD WITH NORTHWARD
INTERPLANETARY MAGNETIC FIELD

SHREE KRISHNA BHATTARAI, Ph.D.

The University of Texas at Arlington, 2013

Supervising Professor: Ramon E. Lopez

The interaction of the solar wind with Earth's magnetic field causes the transfer of momentum and energy from the solar wind to geospace. The study of this interaction is gaining significance as our society is becoming more and more space based, due to which, predicting space weather has become more important. The solar wind interacts with the geomagnetic field primarily via two processes: viscous interaction and the magnetic reconnection. Both of these interactions result in the generation of an electric field in Earth's ionosphere. The overall topology and dynamics of the magnetosphere, as well as the electric field imposed on the ionosphere, vary with speed, density, and magnetic field orientation of the solar wind as well as the conductivity of the ionosphere. In this dissertation, I will examine the role of northward interplanetary magnetic field (IMF) and discuss the global topology of the magnetosphere and the interaction with the ionosphere using results obtained from the Lyon-Fedder-Mobarry (LFM) simulation. The electric potentials imposed on the ionosphere due to viscous interaction and magnetic reconnection are called the viscous and the reconnection potentials, respectively. A proxy to measure the overall effect

of these potentials is to measure the cross polar potential (CPP). The CPP is defined as the difference between the maximum and the minimum of the potential in a given polar ionosphere. I will show results from the LFM simulation showing saturation of the CPP during periods with purely northward IMF of sufficiently large magnitude. I will further show that the viscous potential, which was assumed to be independent of IMF orientation until this work, is reduced during periods of northward IMF. Furthermore, I will also discuss the implications of these results for a simulation of an entire solar rotation.

TABLE OF CONTENTS

LIST OF ILLUSTRATIONS

LIST OF TABLES

CHAPTER 1

INTRODUCTION

1.1 The Sun Earth System

Space physics is the study of interaction of the solar wind with planetary bodies. Those planetary bodies may be magnetized (e.g. Mercury, Earth, Jupiter, Saturn, Uranus and Neptune) or un-magnetized (e.g. Venus and Mars).

This work is focused on the interaction between the Earth's magnetosphere and the solar wind during periods of northward oriented Interplanetary Magnetic Field (IMF). We will examine about changes in the cross polar potential (CPP) (also known as the transpolar potential (TPP)), the four cell convection pattern and the Geoeffective Length due to changing northward IMF parameters.

1.2 Coordinate Systems

Three different coordinate systems are commonly used for the study of interaction of IMF with the Sun-Earth system; the Geocentric Solar Ecliptic (GSE), Geocentric Solar Magnetic (GSM) and Solar Magnetic (SM) coordinates. These coordinate systems have been illustrated in Figure (1.1). Table (1.1) compares and contrasts these coordinate systems.

1.3 The Sun

The Sun is an average sized spherical star containing hot magnetized plasma. The surface temperature of the Sun is about 6000 K, this heat being generated by nuclear fusion of Hydrogen nuclei into Helium at solar core. The radius of the Sun is
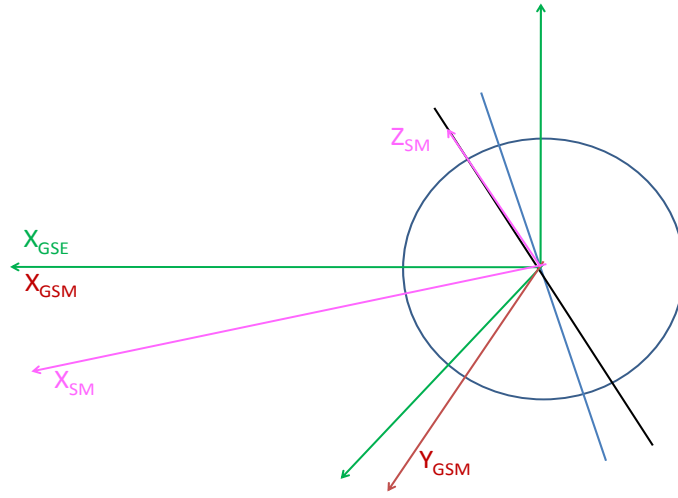
Figure 1.1. Schematic diagram of different coordinate system used. The blue line represents Earth's rotation axis and the black line represents orientation of geomagnetic dipole. Green, Pink and Brown lines represent GSE, SM and GSM coordinate systems respectively. .

Table 1.1. Comparison of coordinate systems used in Space Physics

Coordinates/Orientation	GSE	GSM	SM
X-axis	Sun Earth line	Sun Earth line	Completes right hand rule
Y-axis	Lies in ecliptic plane pointing towards dusk	Perpendicular to plane containing Earth's magnetic dipole pointing towards dusk	Perpendicular to plane containing the dipole axis and the Earth-Sun line and pointing towards dusk
Z-axis	Completes right hand rule (i.e. Parallel to ecliptic pole)	Completes right hand rule (i.e. along magnetic north pole)	Parallel to north magnetic pole

about 218 times the radius of Earth (Re), and its mass about 330,000 times that of Earth. The Sun is located at a distance of approximately 149.6 million kilometers (1

AU) from the Earth. The Sun exhibits a differential rotation pattern completing one rotation about its axis on an average of 28 days, the solar equator and pole completing their rotation at 25 and 35 days respectively [*Philips*, 1995].

The Sun is a magnetically active star with strong and variable magnetic field. The solar magnetic field reverses its polarity every eleven years. Different phenomena in the Sun like the sunspots, solar flares and solar wind occur due to the presence of solar magnetic field. Sunspots are areas on the Sun that appear darker than their surrounding due to its lower temperature but stronger magnetic field, thus reducing the plasma pressure in the spot. This magnetic field causes strong heating of solar corona making corona the source of intense solar flares and coronal mass ejections. A solar flare is a sudden release of charged particle and electromagnetic radiation from the solar surface. Coronal mass ejection (CME) on the other hand are large bubbles of magnetized gases ejected out from the Sun's corona. The Sun, at the same time, also constantly ejects stream of charged particles from its surface, which we call the solar wind.

1.4   The Solar Wind

The solar wind is a stream of quasineutral, ionized, highly conductive and collisionless plasma ejected out from the Sun in all directions. It consist mainly of hydrogen ions (H+), doubly ionized helium ions(He^{2+}) and electrons accelerating outward from solar corona. Solar wind has a nominal speed of 450km/sec with speeds ranging from 300km/sec to 800km/sec [*Hundhausen*, 1995] and nominal density of 6.6 particle/cm^{-3} respectively as it reaches 1 AU, containing approximately 90 percent hydrogen and 9 percent helium ions to make a quasineutral plasma [*Bochsler*, 2000]. The solar wind also carries with it the solar magnetic field, which is called the interplanetary magnetic field (IMF). The interaction of the solar wind and the geo-

magnetic field causes change in the magnetosphere-ionosphere dynamics whose effect can be felt on the surface of the Earth. One of the most common and popular solar wind - geomagnetic field interactions is the formation of aurora at higher latitudes.

Solar wind flow is supersonic and superalfvénic before it reaches the Earth. Solar wind flow is said to be supersonic if it has velocity greater than any pressure wave flow that could exist in the solar wind so as to divert the flow around the magnetosphere. Three common magnetohydrodynamics (MHD) wave mode speeds are the Alfvén speed, sonic (sound) speed and fast magnetosonic speed [*Burgess*, 1995] which are calculated as follows:

$$v_A = \frac{B_{sw}}{\sqrt{\mu_0 \rho_{sw}}} \qquad \text{(Alfvén Speed)} \qquad (1.1)$$

$$C_s = \sqrt{\frac{\gamma P_{sw}}{\rho_{sw}}} \qquad \text{(Sound Speed)} \qquad (1.2)$$

$$v_{MS} = \sqrt{v_A^2 + C_s^2} \qquad \text{(Fast Magnetosonic Speed)} \qquad (1.3)$$

where B_{sw} is the IMF magnitude, ρ_{sw} is the mass density of the solar wind, μ_0 is the permeability of free space, γ is the ratio of specific heats and P_{sw} is the plasma pressure of the solar wind. The ratio of the solar wind speed to Alfvén speed is called the Alfvén mach number and so on. the typical value of Alfvén speed comes for nominal solar wind condition comes out to be 40km/s and the sound speed is also around 40km/sec, but the solar nominal speed is around 400km/sec which gives Alfvén mach number of about 10. So, we can determine Alfvén mach number, Sonic mach number and the fast magnetosonic mach number for a given solar wind condition which have their own significance depending on the region of the magnetosphere.

On the basis of the location of footpoints, three different types of magnetic field lines are possible: A 'closed' field line which has both foot points on the Earth, a 'solar wind/IMF' field line which has both foot points extending to infinity, and, an

'open/reconnected' field line which has one foot point on the Earth and the other extending to infinity.

The solar wind magnetic field may have all possible orientations but in case of Earths' magnetic field, field lines come out from the geographic south pole and end at the geographic north pole. Hence, along the equator, the geomagnetic field always points "up" in all three coordinate systems (i.e., towards the north pole). Thus, any IMF whose magnetic field is similar to Earths' equatorial magnetic field (pointing 'up') is called the northward IMF, the polarity of IMF opposite to northward IMF (i.e. pointing down) would be the southward IMF.

1.5 Bow shock, Magnetosheath, Magnetopause and Magnetosphere

1.5.1 Bow shock

When the supersonic solar wind encounters the geomagnetic field, a shock wave is formed and the solar wind speed decreases to subsonic so that it can turn around the obstacle. The shock wave formed in the dayside in front of the geomagnetic field is called a Bow shock (Figure 1.2). Since the total energy, momentum and mass flow of the solar wind across the shock remains constant, the solar wind plasma turns subsonic and gets heated, compressed and the magnetic field strength increases as it passes through the bow shock. The location of the bow shock depends on the magnetosonic mach number of the solar wind.

1.5.2 Magnetosheath

The region where the solar wind turns subsonic after crossing the bow shock is called the magnetosheath. The shape and size of the magnetosheath depends on magnetosonic mach number and the ram pressure of the solar wind as well as the ionospheric conductivity.
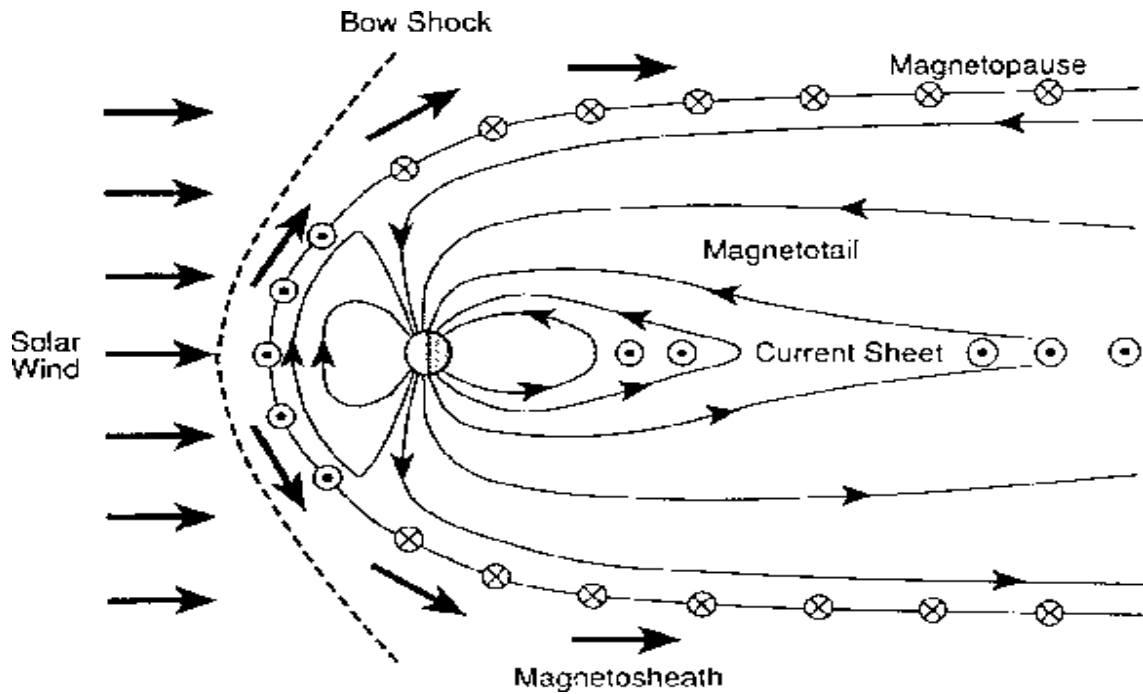
Figure 1.2. Schematic diagram of different regions formed due to IMF-geomagnetic field interaction. The Sun is on the left side of the diagram and the view is along the X-Z plane [*Kivelson and Russel*, 1995].

1.5.3 Magnetopause

The magnetopause is the boundary layer that separates the magnetosphere from the magnetosheath i.e., it is the boundary separating geomagnetic field from the solar wind. As magnetopause separates two regions of different magnetic fields, Amperes' law states that current has to flow along this boundary. This current flowing along the magenopause boundary is known as the Chapman-Ferraro current. The magnetopause current may vary with solar wind dynamic pressure. With higher dynamic pressure, the magnetopause moves closer to the Earth and magnetopause current intensifies causing an increasing in geomagnetic field intensity by tens or even hundreds of nanotesla, which can be measured by ground magnetometers.

1.5.4 The Magnetosphere

The magnetosphere is the region around the Earth where the Earth's magnetic field dominates. From here on, everything we talk about will be related to the Earth's magnetosphere only and hence 'of Earth' will be dropped here after. The overall shape of the magnetosphere depends on the geomagnetic field, the solar wind plasma parameters and the IMF. The magnetosphere is not at all a sphere. The magnetosphere attains a hemispherical shape in the side facing the Sun (also called dayside), but has a cylindrical shape starting from dawn-dusk side towards the night/tail side. The solar wind coming from the Sun compresses the dayside geomagnetic field forming a hemispherical shape along with a cylindrical tail shape on the night side due to draping of the geomagnetic field by the solar wind momentum. Figure (1.2) shows a schematic of different regions formed due to interaction of geomagnetic field with the solar wind IMF.

1.5.5 The Ionosphere

The Ionosphere roughly ranges from 60 to 1000 km from Earth's surface. This region consists of high concentration of electrons due to ionization of gas molecules by solar radiation and hence is electrically conducting. Ionosphere has been further subdivided into D,E and F regions according to different physical process involved in those layers due to varying atmospheric density.

The auroral oval or the auroral zone is one of the regions of ionosphere where the effect of magnetosphere-ionosphere coupling is strikingly visible. The auroral zones lies about 65^0 latitude around both the polar cap and is the region which experiences high degree of ionization due to solar activity. The precipitation of particles in the auroral region produces multi-colored aurora due to optical emission from different gas molecules.
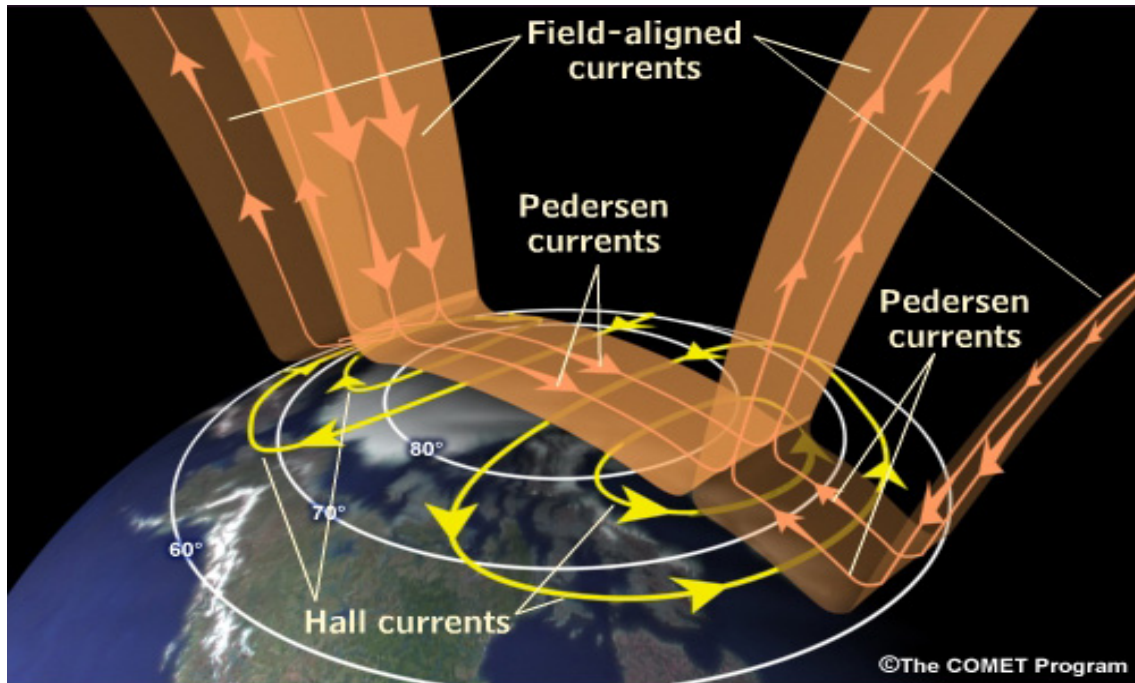
Figure 1.3. Schematic diagram of different types of current system flowing in the polar cap region. The view is from the top of the north pole [https://www.meted.ucar.edu].

Current systems are generated in the magnetosphere due to the forces that create magnetic shear. These currents are called Region I and Region II. They flow along the magnetic field and are collectively called Birkeland currents (Figure 1.3). These magnetospheric currents map down to the ionosphere creating ionospheric current systems,the two important types in the polar cap being the Pedersen and the Hall current. A Pedersen current is parallel to the electric field whereas a Hall current is perpendicular to both the electric field and the magnetic field. The total strength of the interaction is measured in most cases by calculating the potential drop across the polar cap and is known as the cross polar potential (CPP). The CPP is calculated by taking the difference between the highest and the lowest potential generated in a polar cap, although our recent work has shown that it might not be a good proxy to

represent IMF-geomagnetic interaction for certain IMF orientations [*Bhattarai et al.*, 2012; *Lopez et al.*, 2012; *Bhattarai and Lopez*, 2013].

1.6   How does the magnetosphere get its shape ?

In the solar wind, the dynamic pressure (ρu^2) is the major contributor to the total solar wind pressure, with magnetic and thermal pressure contributing around 1% to the total [*Walker and Russell*, 1995]. This solar wind flowing supersonically towards the Earth has to slow down to subsonic speed in order to get around the Earth forming an irreversible (entropy increasing) bow shock. During this transition, the solar wind gets slowed down to subsonic speed, gets compressed and heated and finally reaches the magnetosheath. Thus the contribution to the total solar wind pressure in the magnetosheath due to dynamic, magnetic and thermal components gets altered. As the solar wind passes through the magnetosheath and moving towards the magnetopause, the solar wind gets diverted from the nose towards the flanks creating plasma flow tangential to the magnetopause surface. In the magnetosheath, the plasma thermal pressure gradient is still the dominant force. [*Lopez et al.*, 2010] have studied in detail about the nature of force balance that occurs in the magnetosheath during different solar wind conditions, which will be discussed in detail in upcoming section. At the nose of the magnetopause, the solar wind dynamic pressure balances with the magnetic pressure due to geomagnetic field, i.e.,

$$K\rho_{SW}u_{SW}^2 = B_{MS}^2/2\mu_0 \tag{1.4}$$

where ρ and u represents the solar wind density and velocity respectively, and the subscript SW and MS denotes solar wind and magnetosphere. K is a factor that tell us us how much pressure has been reduced by the divergence of the flow.
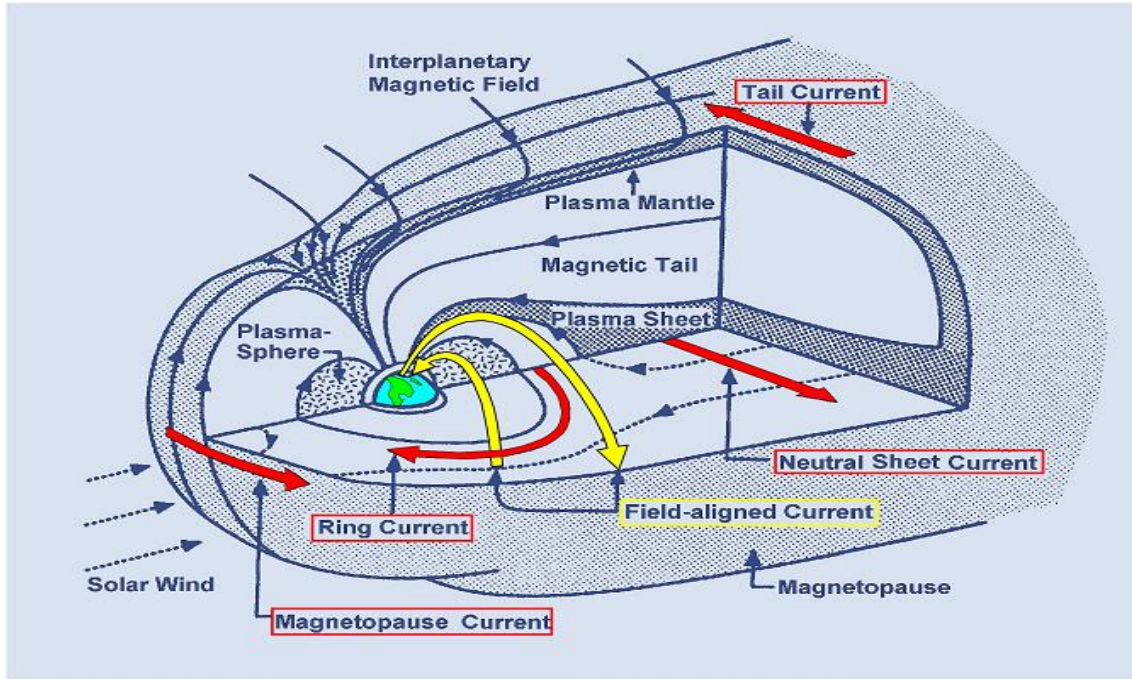
Figure 1.4. Schematics of different types of current system generated in the magnetosphere.

Along the flanks, the solar wind flow is parallel to the geomagnetic field direction and hence the dynamic pressure does not contribute.

It is noteworthy that the magnetic field lines in the two hemispheres are oppositely directed. Hence, according to Amperes' law, a current is created along the boundary separating these two tail lobe regions. This sheet of current formed along the equatorial plane along the tail side is called the current sheet. During steady state there must be a pressure balance between the tail lobe and both the solar wind and the current sheet. The thermal pressure of the ions and electrons in the center of the plasma sheet equates the magnetic pressure of the tail lobes, i.e.,

$$\frac{B_T^2}{2\mu_0} = nk(T_i + T_e) \tag{1.5}$$

where T_i and T_e are the ion and electron temperatures in the current sheets respectively. Every boundary separating plasma of different regimes is characterized by

10

flow of currents in the surface. Thus different type of current systems exists in the magnetosphere-ionosphere system which has been illustrated in figure (1.4). We will discuss these current systems in upcoming chapters according to necessity.

1.7 Methods of Interaction between IMF and geomagnetic field

The circulation of plasma and magnetic field lines within the magnetosphere due to the influence of electromagnetic and/or mechanical force is called plasma convection. There are two basic ways in which interaction between the solar wind and geomagnetic field can take place, the viscous interaction and the magnetic reconnection. These interactions produce convection cells in the magnetosphere that impose electric field in the Earth's polar cap with respect to an observer fixed to the Earth.

When a charged particles enters a region where the magnetic field and the electric field are not aligned with each other, the charged particles experience an unequal force at different parts of its gyration orbit resulting in a net velocity in the direction perpendicular to both the electric and magnetic field, which is called the drift velocity. This drift velocity sets the plasma into a motion whose velocity is given by:

$$v = \frac{\mathbf{E x B}}{B^2} \tag{1.6}$$

As we can see from the equation, the direction of the drift velocity is independent of the charge of the particle. This drift velocity is an important factor while studying the ionospheric flow pattern, and can be used to estimate the magnitude of viscous interaction and magnetic reconnection, which will be discussed in the sections below. It is to be noted that when the observer's frame of reference is moving with the plasma velocity, the observer do not experience the electric field. Hence, when plasma is

moving in the ionosphere, an observer in the Earth would experience an electric field due to this drift motion.

1.7.1 Viscous Interaction

As the solar wind passes through the bow shock, most of the solar wind turns around the Earth and start to attain supersonic speed while moving tailward along the flanks. The velocity shear between the solar wind flowing close to magnetopause and magnetospheric plasma along the flanks at higher latitudes produces Kelvin-Helmholtz waves that cause the magnetospheric plasma to move anti sunward (e.g., [*Otto and Fairfield*, 2000; *Claudepierre et al.*, 2008]). This anti-sunward drag at higher latitude is followed by sunward flow at lower latitude producing a two cell convection pattern [*Axford and Hines*, 1961] as shown in Figure (1.5). The viscous circulation pattern creates a magnetic shear due to the viscous flow. A shear in a magnetic field produces a current in the system, which gets mapped in to the ionosphere where it exerts a force on the plasma producing a circulation pattern in the frame fixed to the (non-rotating) Earth. This electric field can be integrated over a given direction to determine the electric potential imposed in the ionosphere, which we refer to as the viscous potential (VP). Since the viscous interaction is a purely mechanical pheonomena, the orientation of the viscous cells, and hence the electric field, produced in the ionosphere due to viscous interaction is independent of the orientation of IMF. A typical viscous cell is characterized by its presence in the closed field lines regions, and would have a sunward flow at high latitude followed by anti sunward flow in the lower latitudes as shown in figure 1.5.

12
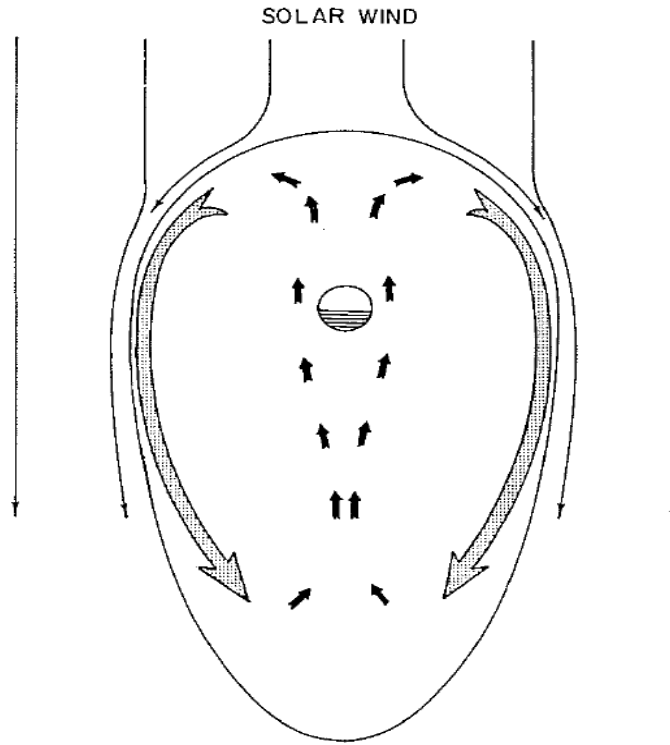
Figure 1.5. A schematic showing the convection pattern created in the magnetosphere due to viscous interaction. The Sun is at the top of the page and the view is of the X-Y plane from above the North Pole.

1.7.2   Magnetic Reconnection

Magnetic reconnection is a process in which plasma from different magnetic domains interact physically thus rearranging the magnetic topology and changing other physical plasma parameters like thermal energy, kinetic energy and particle acceleration. Most of the times in a collisionless plasma, the plasma is considered to be "frozen-in". The frozen-in-flux criterion states that for plasma with very high electrical conductivity, the total magnetic flux through a given surface remains constant even if the surface changes its location or its shape with time. Magnetic reconnection violates the frozen-in-flux condition such that particle exchange can now occur between different flux tubes.

13
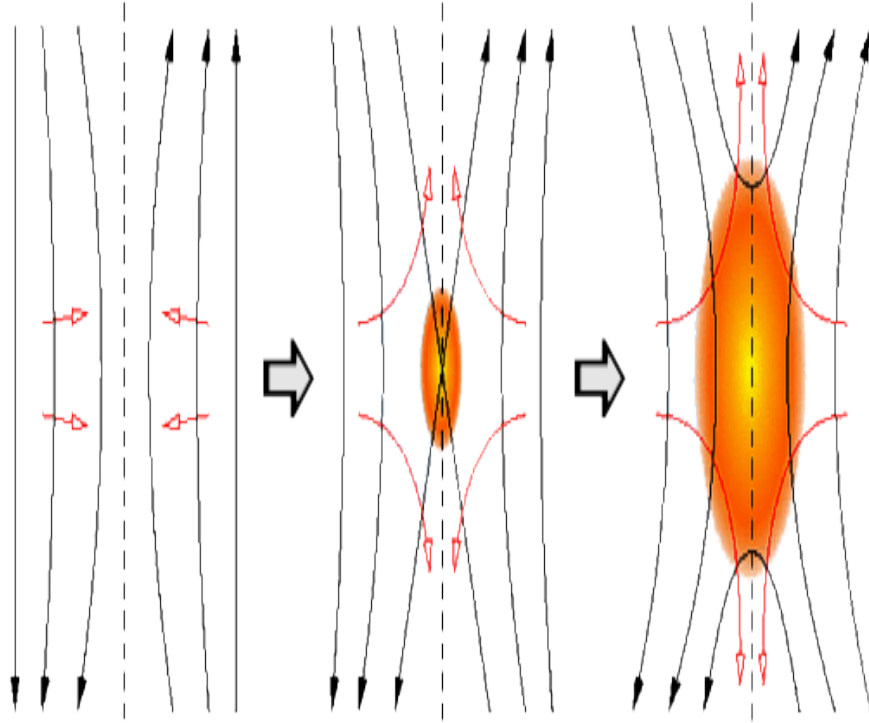
Figure 1.6. Figure showing magnetic reconnection in two-dimensional space.

Figure 1.6 shows schematics of magnetic reconnection in two-dimensional space. Plasma from two different domains having oppositely oriented magnetic field come together and reconnect. During reconnection, the plasma magnetic energy gets converted into thermal and kinetic energy so that the reconnected plasma now has different plasma parameters, kinetic energy and flow direction. Magnetic reconnection is a fundamental process by which magnetic energy is converted into plasma energy.

CHAPTER 2

INTRODUCTION TO THE LFM SIMULATION MODEL

In this chapter, we will discuss about the characteristics of solar wind plasma followed by the discussion of Maxwells' equation describing solar wind plasma. Finally, we will discuss in detail about the fluid based global Lyon Fedder Mobarry (LFM) code that we used for simulating the global Magnetosphere-Ionosphere system.

2.1   Ideal MHD equations for a collisionless plasma

Plasma is a quasineutral gas of charged particles that exhibit collective behaviour. Plasma is a state attained by ionized gases but all ionized gases cannot be called plasma. Quasineutrality of plasma implies that the electron density and the ion density are nearly equal but not so neutral that all the interesting electromagnetic forces vanish. Collective behavior of plasma implies that the motion of the ions depend not only on the local conditions but also on the state of plasma far away from the point of interest [*Chen*, 1974]. An ionized gas can be called plasma if it satisfies the following criterion:

- The gas is electrically neutral on the global scale.
- The Debye shielding (shielding of the external field if present) length is very small compared to the spatial scales under consideration.
- The number of particles on the Debye sphere is substantially large.
- If ω be the frequency of plasma oscillation and τ is the mean time between the colllision with neutral atoms, then $\omega\tau > 1$.

A plasma is said to be colllisionless if the long-range electromagnetic forces are strong enough to neglect the local electromagnetic forces produced due to ordinary local col-

lision. The solar wind is a collisionless, rarefied (less dense) and highly conductive plasma. For a collisionless plasma, the ideal magnetohydrodynamics (MHD) equations are as follows:

$$\frac{\partial \rho}{\partial t} + \nabla \cdot \rho \mathbf{u} = 0 \qquad \text{(Continuity Equation)} \qquad (2.1)$$

$$\rho(\frac{\partial \mathbf{u}}{\partial t} + \mathbf{u} \cdot \nabla \mathbf{u}) = -\nabla \cdot \mathbf{p} + \mathbf{j} \times \mathbf{B} \qquad \text{(Momentum Equation)} \qquad (2.2)$$

$$\nabla \times \mathbf{B} = \mu_0 \mathbf{j} \qquad \text{(Ampere's Law)} \qquad (2.3)$$

$$\frac{\partial \mathbf{B}}{\partial t} = -\nabla \times \mathbf{E} \qquad \text{(Faradays' Law)} \qquad (2.4)$$

$$\mathbf{E} + \mathbf{u} \times \mathbf{B} = 0 \qquad \text{(Frozen} - \text{in flux condition)} \qquad (2.5)$$

where ρ is the mass density, $\mathbf{u}$ is the velocity of the center of mass, $\mathbf{p}$ is the plasma pressure tensor, $\mathbf{j}$ is the current density, μ_0 is the permeability of free space and $\mathbf{B}$ is the magnetic field. Equation (2.1) states that if there is no source or sink on a system, then the rate at which fluids enter the system is equal to the negative of the divergence of the fluid flow. Equation (2.2) deals with the force balance occurring is the system, about which we will be discuss in detail in the upcoming section. Equation (2.3) states that the curl of the magnetic field produces an electric current. The Faradays' equation (Eq.2.4) states that a magnetic field changing with time produces an electric field. The frozen-in flux condition (Eq.2.5) states that the flux through a surface will remain constant even if the surface charges its location and its shape. For a collisionless plasma with extremely high conductivity, Ohms' law changes to the frozen-in flux condition. Now, if the pressure distribution in the system is considered to be isotropic, the pressure tensor $\mathbf{p}$ reduces in to a simple scalar. Using equation (2.3) and (2.5), equation (2.2) and (2.4) takes the form

$$\rho(\frac{\partial \mathbf{u}}{\partial t} + \mathbf{u} \cdot \nabla \mathbf{u}) = -\nabla p - \frac{1}{2\mu_0} \nabla B^2 + \frac{1}{\mu_0}(\mathbf{B} \cdot \nabla)\mathbf{B} \qquad (2.6)$$

$$\frac{\partial \mathbf{B}}{\partial t} = \nabla \times (\mathbf{u} \times \mathbf{B}) \qquad (2.7)$$

16

Thus, equations (2.1), (2.2), (2.3), (2.4), (2.5), (2.6) and (2.7) constitutes seven set of equations with eight unknowns ($\rho, \mathbf{u}, \mathbf{p}, \mathbf{j}, \mathbf{B}, \mathbf{E}, \nabla B^2 and (\mathbf{B} \cdot \nabla)$). Hence we introduce the equation of state assuming the plasma to be a adiabatic gas which relates the pressure and density as

$$\frac{d}{dt}(p\rho^{-\gamma}) = 0 \qquad \text{(equation of state)} \qquad (2.8)$$

where γ is the ratio of the specific heat at constant pressure to the specific heat at constant volume. Equations (2.1), (2.6), (2.7) and (2.8) are the four ideal MHD equations to be solved in order to determine the characteristics of plasma. These four equations are slightly modified in the LFM simulation for some numerical considerations and then solved to obtain a global picture of magnetosphere-ionosphere system [*Lyon et al.*, 2004]. Detail of these modification is discussed in subsection 2.3.4.

2.2 Introduction to Lyon Fedder Mobarry magnetohydrodynamics simulation

All events occurring in the geomagnetic system is controlled by events occurring in the Sun. We are still unable to predict what the Sun is going to do and when that is going to happen. As we can not predict the solar wind parameters, the study of interaction between solar wind and geomanetic field becomes a complex task. Also, in situ measurement of the effect of interaction between the solar wind and the geomagentic field around the Earth simultaneously require lots of satellites at correct place and at correct time which is not economically feasible as well. Thus, a simulation model is required that would allow us to control the input solar wind parameters as well as determine the interaction in the global scale. In this paper, we have used the global Lyon Fedder Mobarry(LFM) magnetohydrodynamics(MHD) simulation model [*Lyon et al.*, 2004]
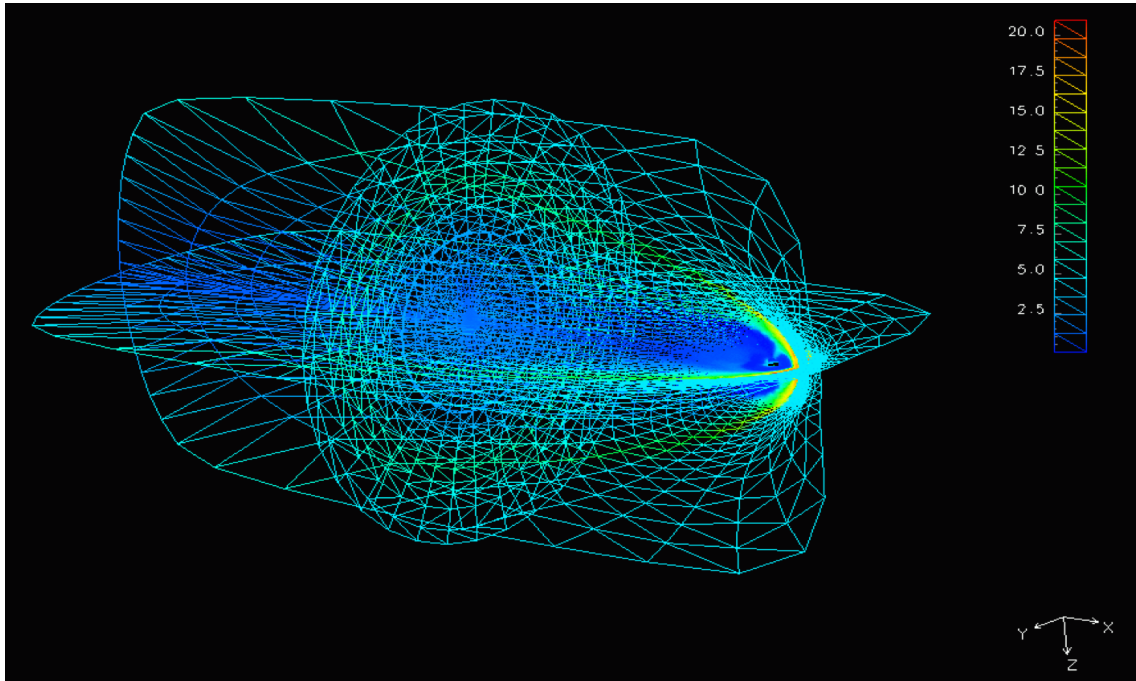
Figure 2.1. The 3-D structure of the LFM simulation grid. The grid density has been color coded..

Figure (2.1) shows the 3-D structure of LFM grid. The grid extends from -30R_E to +100R_E along the Sun-Earth line (X-axis) and 100R_E radially outward from X-axis in Y- and Z- direction. The grid density has been modified such that we get better resolution and finer details at the point of interest such as the bow shock and the magnetopause. The LFM simulation can run ideal as well as real solar wind conditions as input parameters and has been found to produce results that are in agreement with the observations (e.g. [*Lopez et al.*, 2007, 2012; *Lyon et al.*, 1998]) showing LFM to be a reliable model to simulate the magnetosphere-ionosphere system.

2.3   Important features of LFM simulation model

Some of the important features of of LFM simulation model that makes it an useful tool to simulate the global magnetosphere ionosphere system are described below.

2.3.1   LFM grid

LFM uses a non adaptive distorted spherical grid (i.e. the grid shape and size does not change while the simulation is running) with a predetermined shape and size (Figure (2.1) and (2.2)). The (r, θ) component of the grid is adapted to the nature of the problem whereas the ϕ component is not adapted but stretched slightly with bigger cell size along equator but smaller cell size (denser cell spacing) along the north and south poles for better ionospheric mapping. The "weighted smoothness integral" method is applied to find the grid coordinates along the (r, θ) direction and is adjusted such that we have higher grid resolution near the magnetopause, bow shock and the tail [*Lyon et al.*, 2004] and references therein]. In LFM, the axis of the cylinder lies in equatorial plane and the magnetic dipole is always perpendicular to this plane. This implies that the input solar wind condition should always be in SM coordinate system.

2.3.2 $\nabla \cdot \mathbf{B} = 0$

The maxwell equations clearly state $\nabla \cdot \mathbf{B} = 0$, one of the constraints in the nature of magnetic field, and has to be conserved at all times. There is always a possibility of having a finite $\nabla \cdot \mathbf{B}$ due to numerical errors, which implies magnetic helicity. This problem has been dealt in different ways by different MHD model developers. *Powell et al.* [1999] dealt with this problem by allowing a finite $\nabla \cdot \mathbf{B}$ arising due to numerical errors but adding $-\nabla \cdot \mathbf{B}$ term on the momentum equation

19
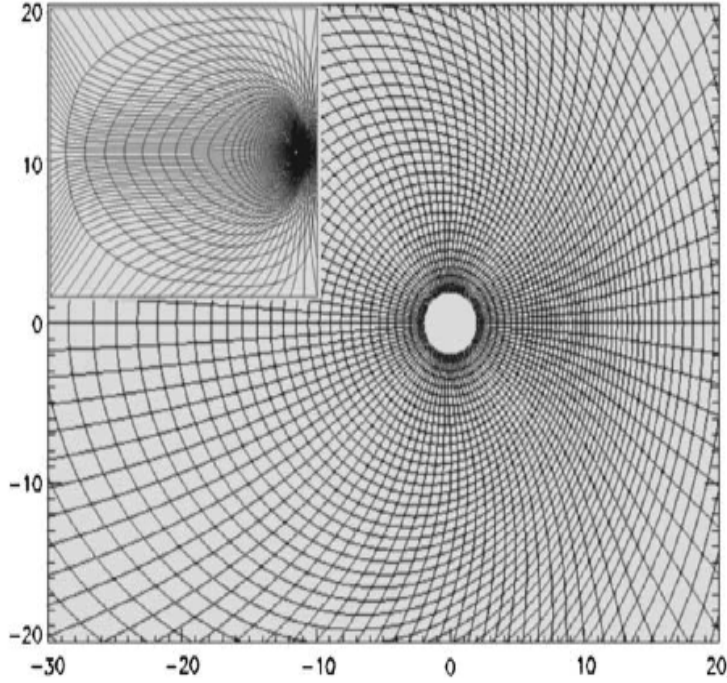
Figure 2.2. A typical LFM magnetosphere grid is shown in the inset along with a blow-up of the grid around the Earth is shown in the larger image [*Lyon et al.*, 2004].

(2.2) and Faradays' law (2.4). The additional term canceled out the overall effects but still left the MHD equations with subtle problems like existence of non-physical forces along magnetic field lines [*Lyon et al.*, 2004].

The global LFM MHD simulation code uses total variation diminishing (TVD) scheme with cell-centered quantities for propagation of the fluid in the system. It was found that the TVD algorithms yields a non-zero $(\nabla \cdot \nabla \times)$ value but later on it was found that TVD would work if the "Yee grid" was used [*Lyon et al.*, 2004].

2.3.3 Boris Correction

In a numerical simulation, the time step should be less than the time taken by a wave to travel between two adjacent cells [*Courant et al.*, 1928]. In LFM simulation,

20

Alfvén wave is the limiter. Plasma near the near Earth region and in the tail lobes have high Alfvénic values (refer figure 2.2), thus requiring the simulation to have really smaller time step making it computationally intensive and impractical. In the near Earth region, the inner boundary of the LFM is set about 3.5 R_E thus resolving this issue. But in the tail region, truncating the simulation domain can not be a option so that the other solution is to find a method to increase the length of time step, which has been acheived using Boris correction [*Boris*, 1970]. The Alfvén speed is limited by the displacement current to the speed of light, as can be seen from Amperes law. Thus, we include the displacement current in the momentum equation (2.2) to attain this limit [*Lyon et al.*, 2004]. Also, by deceasing the speed of light in the simulation , the time step in the lobe cells may be lengthened. Hence, the LFM simulation is set to run so that the speed of light is $1.1 \times 10^8 cm/s$.

2.3.4   The plasma energy equation

As discussed in section (2.1), the ideal MHD equations have to be modified in the LFM simulation due to numerical consideration as some of the conservation equation may not be conservative. For example, the total energy conservation equation is replaced by plasma energy conservation equation as total energy equation has drawbacks in a some regions of the magnetosphere [*Lyon et al.*, 2004]. The energy conservation equation is obtained by dotting velocity with equation (2.6).

$$\frac{\partial}{\partial t}(\frac{\rho u^2}{2} + \frac{p}{\gamma - 1} + \frac{B^2}{2\mu_0}) + \nabla \cdot (\frac{\rho u^2}{2}\mathbf{u} + \frac{\gamma}{\gamma - 1}p\mathbf{u} + \frac{\mathbf{E} \times \mathbf{B}}{\mu_0}) = 0 \text{ (Total Energy Eq.)}$$

$$(2.9)$$

Equation (2.9) contains a mixture of plasma energy and magnetic energy term which can be further re-written so that the plasma energy term is in the left side as follows:

$$\frac{\partial}{\partial t}(\frac{\rho u^2}{2} + \frac{p}{\gamma - 1}) = -\nabla \cdot (\frac{\rho u^2}{2}\mathbf{u} + \frac{\gamma}{\gamma - 1}p\mathbf{u}) + \mathbf{j} \cdot \mathbf{E} \text{ (Plasma Energy Eq.)} \quad (2.10)$$

Thus *Lyon et al.* [2004] have come out with four basic equations that is being solved in the global LFM simulation:

$$\frac{\partial \rho}{\partial t} + \nabla \cdot \rho \mathbf{u} = 0 \qquad \text{(Continuity Equation)}$$

(2.11)

$$\frac{\partial \rho u}{\partial t} = -\nabla \cdot (\rho \mathbf{u}\mathbf{u} + \underline{I}P) - \nabla \cdot (\underline{I}\frac{B^2}{8\pi} - \frac{\mathbf{B}\mathbf{B}}{4\pi}) \qquad \text{(monemtum equation)}$$

(2.12)

$$\frac{\partial E_p}{\partial t} = -\nabla \cdot (\mathbf{u}(\frac{\rho u^2}{2} + \frac{\gamma}{\gamma - 1}P)) - \mathbf{u} \cdot \nabla \cdot (\underline{I}\frac{B^2}{8\pi} - \frac{\mathbf{B}\mathbf{B}}{4\pi}) \quad \text{(plasma energy equation)}$$

(2.13)

$$\frac{\partial B}{\partial t} = \nabla \times (\mathbf{u} \times \mathbf{B}) \qquad \text{(Faraday's Law)}$$

(2.14)

where $E_p = (\frac{\rho u^2}{2} + \frac{P}{\gamma - 1})$ and $\underline{I}$ is a unitary tensor.

2.3.5   Ionosphere in LFM

As stated in Section (2.3.3), the LFM inner boundary is set to about 3.5 R_E below which the magnetosphere is coupled to ionosphere. Ionospheric conductivity is introduced in the inner boundary (below 3.5 R_E) in order to measure the magnetosphere ionosphere coupling. The ionospheric potential is solved using the thin spherical shell assumption:

$$\nabla \cdot \underline{\Sigma} \cdot \nabla \psi = j_{||} sin\delta \qquad (2.15)$$

where,

$$\underline{\Sigma} = \begin{pmatrix} \Sigma_P/sin^2\delta & -\Sigma_H/sin\delta \\ \Sigma_H/sin\delta & \Sigma_P \end{pmatrix}, \qquad (2.16)$$

where Σ is the conductivity tensor, δ is the dip angle, ψ is the electrostatic potential and Σ_P and Σ_H are the Pedersen and Hall conductivities respectively. For our current

22

"stand-alone" LFM simulation, two types of conductivity model are available. The first model assumes a temporally and spatially constant conductance and hence uses a uniform height integrated condutance to solve for the ionospheric potential. The second is a semi-empirical model that uses solar extreme ultraviolet (EUV) irradiance and auroral precipitation as input with EUV flux at the 10.7 cm line varying in space with respect to solar zenith angle. The auroral component in LFM is further calculated using the electron precipitation at the inner boundary and the field-aligned current [*Fedder et al.*, 1995, Equation 3, 4 and 5],[*Mitchell et al.*, 2010]. Thus the total conductance in this case is the square root of the sum of the squares of conductivities due to auroral precipitation and EUV flux.

The ionospheric conductivity as described by Equation(2.16) is a tensor quantity. For uniform and isotropic distribution of conductance, Equation (2.15) reduces to a simple Poisson equation for potential. In LFM simulation, the Birkeland current is mapped directly from 3.5 R_E to the ionosphere, where Equation (2.15) is solved and the electric field is calculated. This electric field is mapped back along the magnetic field to the inner LFM boundary to determine boundary conditions for the plasma flow, as given by the EXB flow condition, in the LFM simulation.

2.4   Methods of Visualizing LFM data

The LFM simulation produces data in hierarchal data format (HDF) files. Contents of this file varies with the version of LFM simulation code used but it basically contains the LFM grid (which is fixed in time), the solar wind density, velocity, sound speed, and the magnetic field at cell centers as well as the magnetic fluxes and electric fields on the cell surfaces for each time step. Also the HDF file contains information about the field-aligned currents, ionospheric potential, Pedersen and Hall conductances, particle energy and fluxes for each hemisephere for a given time step.

There are different visualization software that can be used to read the HDF file and create plots, we use CISM-DX in our case. CISM-DX is a modified version of open-DX created by IBM and was later developed as open source [*Wiltberger et al.*, 2005]. All the simulation plots created in this work have been created using CISM-DX.

CHAPTER 3

SATURATION OF THE CROSS POLAR POTENTIAL DURING PURELY
NORTHWARD IMF

In this chapter we analyze results obtained from the LFM simulation showing
a typical four cell convection pattern generated in each hemisphere during northward
IMF followed by evidence showing saturation of the CPP during purely northward
IMF from LFM simulation and from the satellite data obtained from defense meteo-
rological satellite program (DMSP). We will further demonstrate that the saturation
of the CPP during northward IMF can be better explained using magnetosheath force
balance model proposed by *Lopez et al.* [2010].

3.1   The Cross Polar Potential (CPP)

As discussed in previous chapters, the interaction of the solar wind with the
geomagnetic field causes transfer of mass, energy and momentum to the geomagnetic
system. One of the methods to measure this interaction is by measuring the CPP
imposed onto the Earths' hemispheres. The CPP is defined as the difference between
the maximum and the minimum potential present in the dawn/dusk side in a given
hemisphere. The measurement of the CPP has been considered as the most basic way
of measuring the magnetosphere-ionosphere interaction for all IMF orientations. But,
in the upcoming sections, we will discuss and show that during periods with northward
IMF the measurement of the CPP does not fully incorporate all the interactions
present in the geomagnetic system.
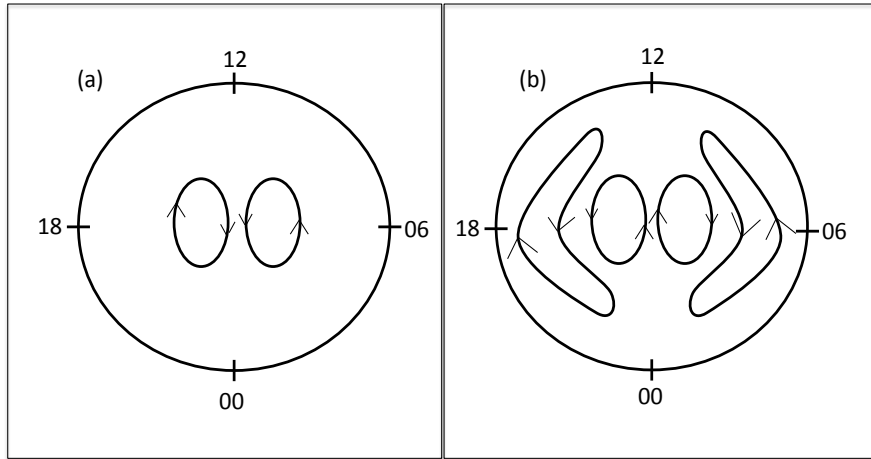
Figure 3.1. A schematic of the two cell and four cell convection patterns for (a) south-ward and (b) northward interplanetary magnetic field (IMF), respectively [*Bhattarai et al.*, 2012].
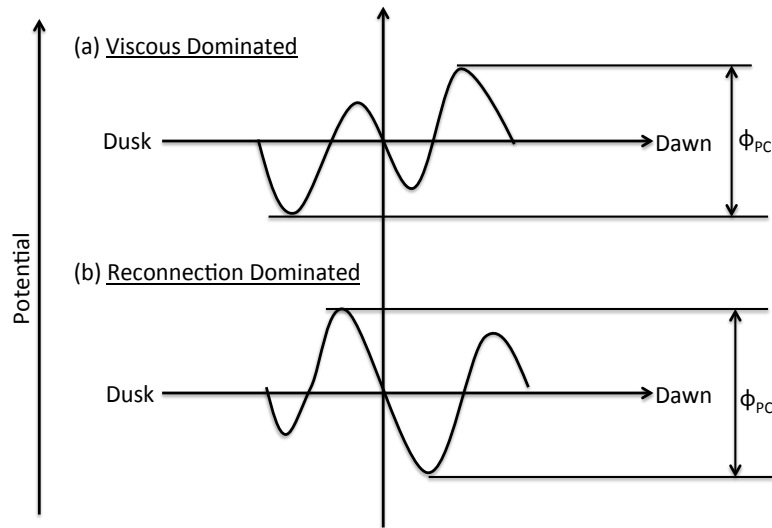
Figure 3.2. A schematic showing the variation of potential pattern if a satellite were to fly right through the maxima/minima of the four-cell convection pattern as shown in Figure (3.1)(b) [*Bhattarai et al.*, 2012].

3.2 The four cell convection pattern

Figure (3.1) represents a typical cartoon of (a) a two cell and (b) a four cell convection pattern formed in the ionosphere during purely southward and northward IMF orientations respectively. For both the figures the Sun is at the top of the page. When the IMF is southward, the viscous and the reconnection cells formed in the magnetosphere convects in the same direction and also do overlap which when mapped into the ionosphere via magnetic field lines forms a typical two cell convection pattern in the ionosphere. But when the IMF is northward, the magnetic reconnection occur poleward of the cusp region [*Dungey*, 1961; *Song et al.*, 2000] forming the reconnection cells closer to the poles and on open field lines. This produces two new reconnection cells in the open field lines alongside with the viscous cells formed in closed field lines. Also, the plasma convection pattern in the viscous and the reconnection cell are oppositely oriented due to sunward flow of plasma during magnetic reconnection. This reconnection cell has a sunward flow at higher latitude followed by a antisunward flow at lower latitude, exactly opposite to the orientation of the convection pattern due to the viscous interaction. These sunward reconnection cells formed in the case of northward IMF are also referred as reverse convection cells. The idea of the four cell convection pattern during northward IMF has been proposed by many authors [e.g., *Burke et al.*, 1979; *Crooker*, 1992; *Cumnock et al.*, 1995]. The existence of the four cell convection pattern in the ionosphere has also been shown by *Huang et al.* [2000] using the SuperDARN (Super Dual Auroral Network), a ground based RADAR system; and also by *Sundberg et al.* [2009a] using the DMSP (Defense Meteorological Satellite Program) satellite data.

Figure (3.2) shows the potential pattern we would observe if we were to perform an artificial fly-through along the dawn dusk line right through the center of the convection cells during a four cell convection pattern. The y-axis represents the

electric potential that would be measured during this fly through. The inner two cells in this figure corresponds to the reverse convection potential, and the outer cells are due to the viscous interaction. The ϕ_{PC} in Figure (3.2) shows two different ways in which the CPP would be measured during northward IMF. It is obvious from this figure that depending on the magnitude of B_z, we will either be measuring the viscous potential or the reverse convection potential depending on the IMF B_z value. One important observation we can make with this potential variation pattern is that the viscous potential and the reverse convection potential are separable in the case of purely northward IMF. This dissociative property of the viscous and the reconnection cell during the northward IMF will be utilized to demonstrate reduction of the viscous potential in Chapter 4, and the measurement of geoeffective length during the reconnection-dominated regime (section 3.3.1) before the CPP gets saturated.

3.3   The saturation of the CPP during northward IMF

The CPP is said to be saturated if it stops responding to an increasing magnitude of the IMF above a certain IMF value. The saturation of the CPP during periods of strong northward IMF has been shown by different authors using different techniques. *Wilder et al.* [2008, 2009] used SuperDARN data, and [*Sundberg et al.*, 2009a] used a DMSP satellite data and reported the saturation of the CPP for northward IMF. *Sundberg et al.* [2009a] in particular have reported saturation when the CPP reaches to about 60 kV, corresponding to the IMF B_z between 10-15 nT.

Figure (3.3) shows that as B_z increases, the CPP starts to decrease, attains a minimum value and then finally starts to increase. Based on this variation pattern, we can separate the variation of the CPP with B_z into two different regimes, the viscous dominated and the reconnection dominated regime. The reconnection regime can be further divided into the linear and the saturation regime. The separation of the
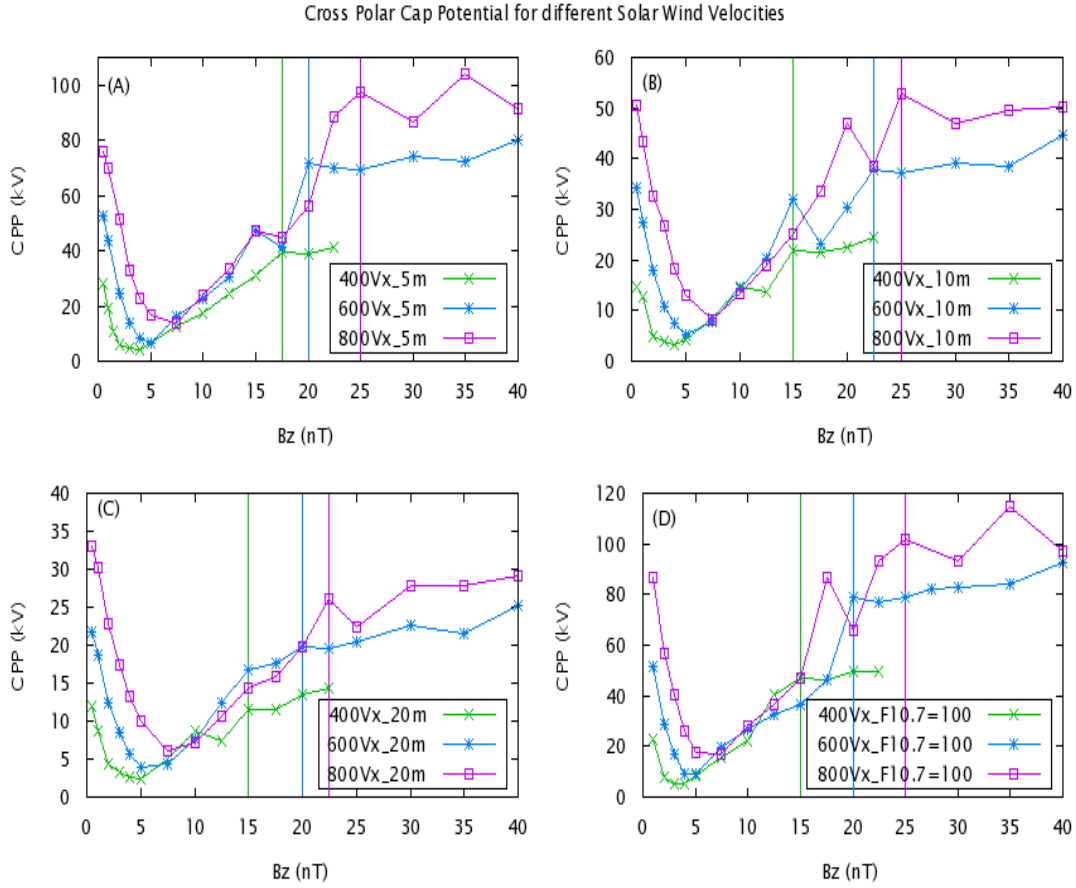
Figure 3.3. Result obtained from LFM simulation showing the variation fo the CPP as a function of IMF B_z for various solar wind velocities.(A-C) shows CPP for uniform ionospheric conductivities of 5, 10 and 20 mhos. (D) shows results obtained by using the ionospheric conductivity model with the F10.7 value of 100. The vertical lines of a given color separate the linear regime from the saturation regime for simulation results denoted by that color [*Bhattarai et al.*, 2012].

viscous and reconnection dominated regimes depends on the value of B_z at which the reverse convection potential becomes greater than the viscous potential, as explained in the discussion of Figure (3.2). For all runs with B_z less than 4 nT, we see that the CPP is decreasing, which implies that the viscous potential is decreasing with increasing magnitude of B_z but the reconnection potential has not become strong enough to exceed the reduced viscous potential value. Once the CPP reaches the

minima, the value starts to increase with increasing B_z. So at this point, the reverse convection potential becomes stronger than the viscous potential and hence the graph switches from the viscous dominated to the reconnection dominated regime. For all CPP readings after the minima, the CPP we will be measuring is actully just the reverse convection potential. This reverse convection potential will increase further on increasing B_z, but after a certain point the reverse convection potential does not respond as much, showing the saturation of the CPP during northward IMF. Furthermore Figure (3.3) also shows that the value of B_z at which the CPP attains the minimum potential increases with increasing solar wind velocity. This happens because the viscous potential increases with increasing solar wind velocity [e.g., *Newell et al.*, 2008; *Bruntz et al.*, 2012a] so that higher B_z is required to generate reconnection potential large enough to exceed the viscous potential.

Figure (3.3) shows results obtained from LFM simulation showing saturation of the CPP for purely northward IMF during various solar wind velocity and ionospheric conductivity conditions. Figure (A), (B) and (C) shows saturation of the CPP during uniform ionospheric conductivites of 5, 10 and 20 mhos, while (D) shows saturation of the CPP with the ionospheric conductivity model turned on with F10.7 value of 100. The vertical lines of a given color separates the linear reconnection regime from the saturation regime for the identically colored simulation results. The CPP value of the LFM result for $V_x = 400$ km/s contains data only up to B_z=22.5 nT as runs with B_z greater than 22.5 nT resulted in the bowshock forming out of the simulation grid due to low mach number, and hence those results were unreliable.

Figure (3.4) shows a different view of the same data used to create Figure (3.3). Figure (A), (B) and (C) shows the variation of the CPP with increasing Bz during constant solar wind speed of 400, 600 and 800 km/sec respectively. In this figure we see that the minima occurs at the same value of B_z, independent of ionospheric
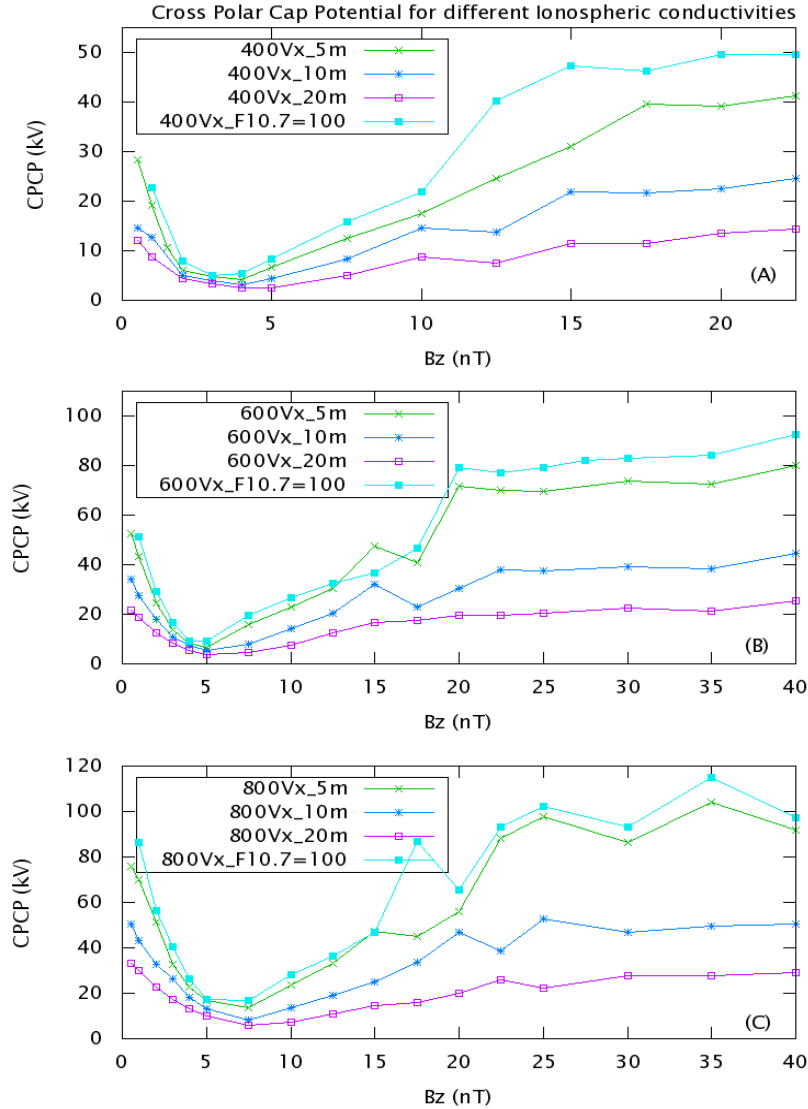
Figure 3.4. Result obtained from LFM simulation showing the variation fo the CPP as a function of IMF B_z for various solar wind velocities. The figure is a rearrangement of figure 3.3 and shows the dependence the saturation value on the ionospheric conductivity during a constant solar wind speed [*Bhattarai et al.*, 2012].

conductivity but the value of B_z at which the minima occur increases with increasing solar wind speed. This happens because higher solar wind speed implies higher viscous potential, and hence stronger B_z is required to exceed the viscous value. We also see that the CPP is larger for lower ionospheric conductivity for a given solar wind speed

because lower conductivity requires a larger potential to drive the current through the ionosphere.

Figure (3.5) shows the results obtained from the DMSP F-13 satellite showing saturation of the CPP during periods of northward B_z. The white line denotes an envelop showing the trend line of the maximum potential as seen by the DMSP satellite during northward IMF. These data point were collected during periods when the IMF was northward and B_y was low for at least 90 minutes to ensure that we do not have any effect of southward Bz remaining in the magnetosphere-ionosphere system. The white trendline in the figure suggests that the CPP decreases with increasing B_z, attains a minimum value and then starts increasing, exactly as seen from the LFM simulation (Figure (3.3)). The saturation potential is seen to be about 60 kV. The list of dates analyzed from the DMSP satellite and the value of the potentials obtained is listed in appendix A.1 and the detail procedure obtaining the CPP value from DMSP is discussed in appendix B.1.

3.3.1 The geoeffective length during northward IMF

As the solar wind flows towards the Earth, only a small portion of the flow interacts with the geomagnetic system, and an even smaller portion gets reconnected with the geomagnetic field. The fraction of the solar wind that gets reconnected can be expressed as a length which is perpendicular to both the solar wind flow as well as the IMF orientation, the geoeffective length. Thus for northward IMF, the geoeffective length is the Y-axis length through which if the solar wind passes, it will merge with the geomagnetic field. The reconnection dominated linear regime in Figure (3.3) shows the change in reconnection potential with changing B_z during
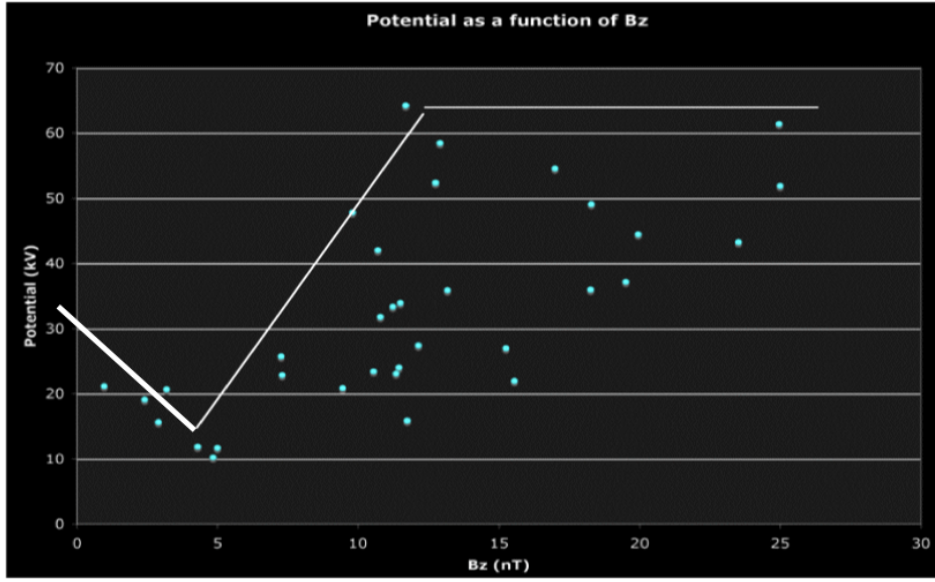
Figure 3.5. Result obtained from DMSP satellite showing variation of the CPP during periods of northward IMF. The white line is an envelop showing maximum value of the potential seen by the DMSP satellite.

LFM simulation. From this data we can use the following formula to determine the geoeffective length during northward IMF:

$$\phi_r = V_x B_z L_G \tag{3.1}$$

where $\phi_{(r)}$, V_x and B_z are the reconnection potential, the solar wind flow velocity and magnetic field respectively, and L_G is the geoeffective length. Once the CPP saturates, the total CPP remains fairly constant. In that case, the above equation can be rewritten as:

$$\phi_r = V_x B_z L_G \simeq V_x B_z (L_s B_s / B_z) \tag{3.2}$$

where L_s is the geoeffective length during saturation and B_s is the value of the magnetic field when the CPP saturates. This implies that after saturation the increasing B_z reduces the geoeffective length such that the CPP remains constant.

33

Table 3.1. Variation of geoeffective length for different values of solar wind velocity and ionospheric conductivity.

Solar wind	Slope of linear regime (kV/nT)			Geoeffective length (Re)		
(km/s)	5 mhos	10 mhos	20 mhos	5 mhos	10 mhos	20 mhos
400	2.44	2.04	0.8	0.96	0.80	0.31
600	3.19	2.45	1.18	0.83	0.64	0.3
800	3.91	2.54	1.28	0.77	0.5	0.25

Table 3.1 shows the variation of geoeffective length with solar wind speed during different ionospheric conductivity. For ionospheric conductivites of 5 and 20 mhos, the geoeffective length is seen to decrease by a factor of 1.24 when solar wind velocity increase from 400 to 800km/s; whereas for the ionospheric conductivity of 10 mhos, the geoeffective length decreases by a factor of 1.6 for the same increase in the solar wind velocity. This shows that the decrease in geoeffective length with solar wind speed is a non-linear phenomena and depends on the ionospheric conductivity. The table also shows that the geoeffective length decrease with increasing solar wind speed for a given ionospheric conductivity.

3.3.2 The magnetosheath force balance during northward IMF

The saturation of the CPP during southward IMF has been shown by different authors using different methods. *Russell et al.* [2001]; *Liemohn et al.* [2002] used the assimilated mapping of ionospheric electrodynamics (AMIE) potential data, and *Shepherd et al.* [2002] used the high-latitude radar observation of the ionospheric flows to show the saturation. *Hairston et al.* [2003]; *Ober and Burke* [2003] used the DMSP data to show the saturation of the CPP during southward IMF. The saturation of the CPP has also been seen in various global MHD codes [e.g., *Raeder et al.*, 2001], and also in the LFM simulation code [e.g., *Merkin et al.*, 2003; *Lopez et al.*, 2009, 2010].

A number of models have been put forward to explain the saturation of the CPP during southward IMF periods. *Hill et al.* [1976]; *Siscoe et al.* [2002a,b] proposed the weakening of the Region 1 current with increasing IMF magnitude. Region 1 current are sheets of current on the high latitude side of the auroral zone, which enters the ionosphere from the dusk side, moves across the polar cap, and comes out from the dawn side. The region 1 current is driven by the interaction between the solar wind and geomagnetic field.*Ridley* [2007]; *Kivelson and Ridley* [2008] proposed the development of the Alvén wings during low solar wind Alvén mach number flows. *Merkin et al.* [2003]; *Mekin et al.* [2007] suggested the change in magnetosheath thickness and magnetopause shape causing the saturation phenomena. *Raeder et al.* [2001] suggested that the dayside magnetosphere changes its configuration by choking off the merging region thereby causing saturation of the CPP for higher B_z.

The Siscoe-Hill model [*Siscoe et al.*, 2002a] assumes that the CPP is limited by the total amount of Birkeland current required to stand off the $\vec{\mathbf{J}} \times \vec{\mathbf{B}}$ force. Now, during northward IMF, the merging rate, and thus the geoeffective length, is significantly low so that a larger B_z is required to attain saturation. But from observation [*Wilder et al.*, 2010] as well as from simulation[*Bhattarai et al.*, 2012], we see that the value of the CPP is lower compared to southward IMF, implying that the Siscoe-Hill model is not correct for northward IMF. The Alfveń wing model on the other hand does not explain about the variation of the geoeffective length with B_z during the linear regime and only operates during low mach number flow, hence completely missing the linear regime.

Lopez et al. [2010] proposed the magnetosheath force balance model to explain the saturation of the CPP during periods of southward IMF where they showed that the portion of reconnection potential that contribute to the CPP is controlled

by the divergence of the plasma in the magnetosheath. The force balance in the magnetosphere can be understood with the following equation:

$$\rho \frac{d\vec{V}}{dt} = -\nabla P + \vec{J} \times \vec{B} \tag{3.3}$$

where ρ is the plasma density, V is plasma velocity, P is the plasma pressure, $\mathbf{J}$ is the current density and $\mathbf{B}$ is the magnetic field. Usually, the gradient of the plasma pressure controls plasma flow in the magnetosheath (equation 3.3). But, as the magnetic field gets stronger, the $\vec{J} \times \vec{B}$ term starts to get bigger and finally dominates over the gradient of plasma pressure (∇P) term. At this point, a further increase in IMF magnitude causes more flow to divert from the merging region, thus decreasing the geoeffective length with increasing B_z and maintaining the same flux entering the merging region and hence the same reconnection potential, resulting in the saturation of the CPP. According to the force balance model, the magnetosphere transitions from linear to the saturation regime once the magnetic force begin to dominate the pressure gradient force in the magnetosheath. This transition point can be found by calculating the plasma β (equation 3.4), the ratio of the plasma pressure to the magnetic pressure. The transition from linear to saturation regime starts when plasma beta reaches one.

$$\beta = \frac{2\mu_0 P}{B^2} \tag{3.4}$$

Figure (3.6) shows result obtained from the LFM simulation showing the variation of plasma beta in X-Z plane during purely northward IMF magnitudes of (a,b) 7.5 nT, (c,d) 12.5 nT and (e,f) 17.5 nT for two different solar wind velocities of 400 and 800km/s. Both the runs have solar wind density of 5/cc and the ionospheric conductivity of 10 mhos. For solar wind speed of 400km/sec, we see that the plasma beta in the magnetosheath is greater than one for B_z of 7.5 and 12.5 nT but beta

Table 3.2. Range of solar wind IMF values when the magnetosheath transitions from being pressure dominated to magnetically dominated for different values of solar wind speed and ionospheric conductivites [*Bhattarai et al.*, 2012].

Solar wind	Values of B_z (in nT) when plasma beta transitions from less than one to greater than one			
(km/s)	5 mhos	10 mhos	20 mhos	F10.7=100
400	12.5-15	12.5-15	12.5-15	10-12.5
600	17.5-20	17.5-20	15-17.5	15-17.5
800	20-22.5	22.5-25	20-22.5	20-22.5

drops below one for B_z of 17.5 nT, showing saturation. When the solar wind speed is 800km/s, we see that the plasma beta remains greater than one for B_z of 17.5 nT showing that the saturation will occur for B_z values higher than 17.5 nT. This higher B_z requirement for higher solar wind velocity can be explained using the magnetosheath force balance concept. As the velocity increases, the plasma pressure will also increase, thus for higher plasma pressure higher B_z is required to obtain the beta value of one, as plasma beta is the ratio of plasma pressure to magnetic pressure. Figure (3.3) shows the saturation of the CPP at a B_z value of 25 nT for solar wind speed of 800km/s and ionospheric conductivity of 10 mhos.

Table 3.2 shows the range of B_z when plasma beta transitions from greater than one to less than one for different ionospheric conductivity values. These values were obtained by analyzing the X-Z cut plane as in Figure (3.6) using CISM-DX. The vertical lines of respective color in Figure (3.3) also shows us an approximate boundary where the CPP transits from the linear to the saturation regime.

Figure (3.7) compares solar wind density and plasma pressure of two LFM runs for same IMF value of 7.5 nT with solar wind speeds of 400 and 800 km/s, all other parameters remaining constant. We can clearly see from the figure that as the solar wind speed increases, it has higher plasma density distribution in the magnetosheath
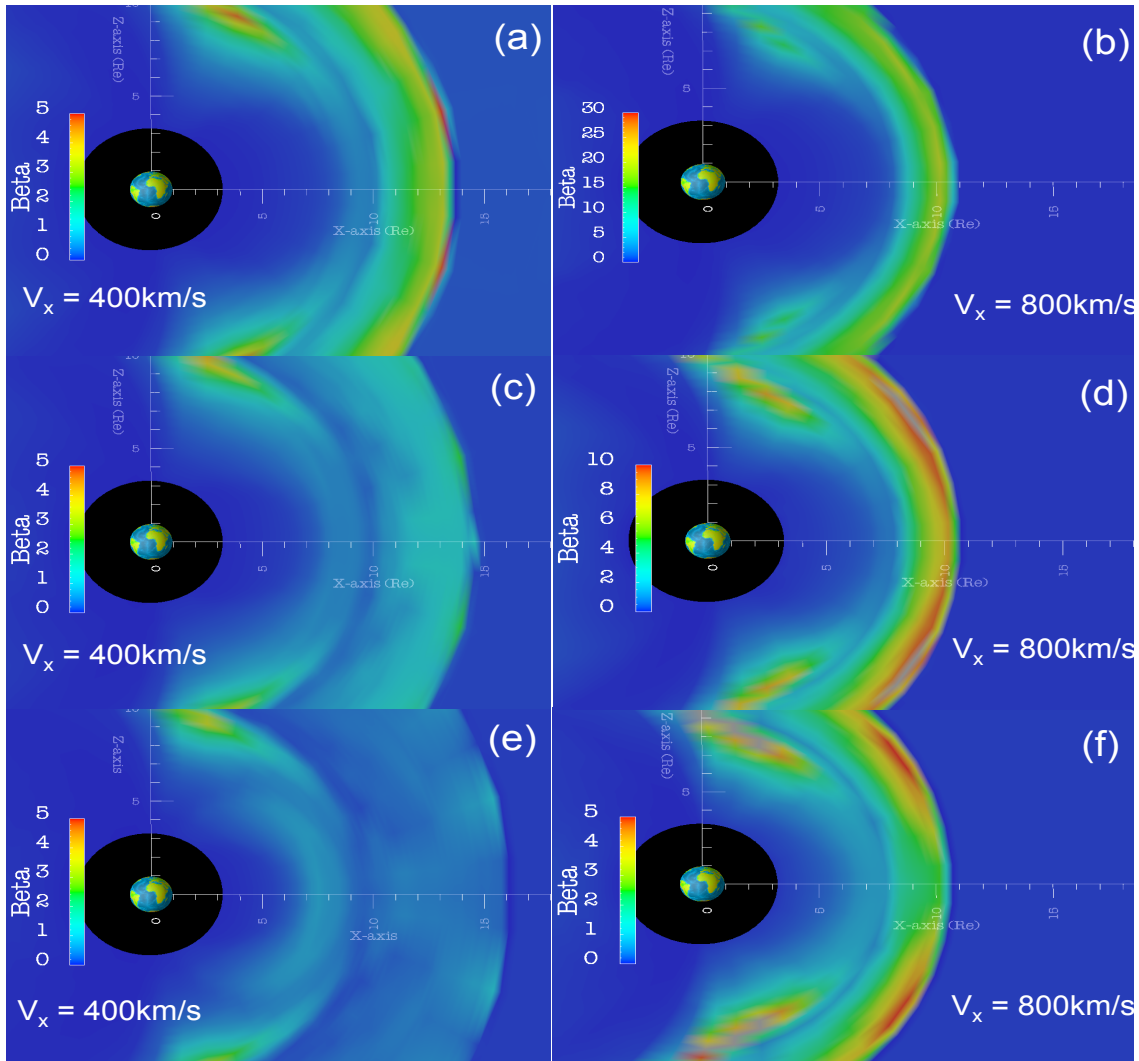
Figure 3.6. Result obtained from LFM simulation showing the variation of plasma beta in X-Z plane during purely northward IMF magnitudes of (a,b) 7.5 nT, (c,d) 12.5 nT and (e,f) 17.5 nT for two different solar wind velocities of 400 and 800km/s. Both runs have solar wind density of 5/cc and the ionospheric conductivity of 10 mhos[*Bhattarai et al.*, 2012].

suggesting a higher pile up of plasma in the magnetosheath region. Also, the plasma pressure in the magnetosheath is seen to be strikingly high for 800km/s sec. This proves our previous claim that for higher solar wind velocities, a higher value of IMF
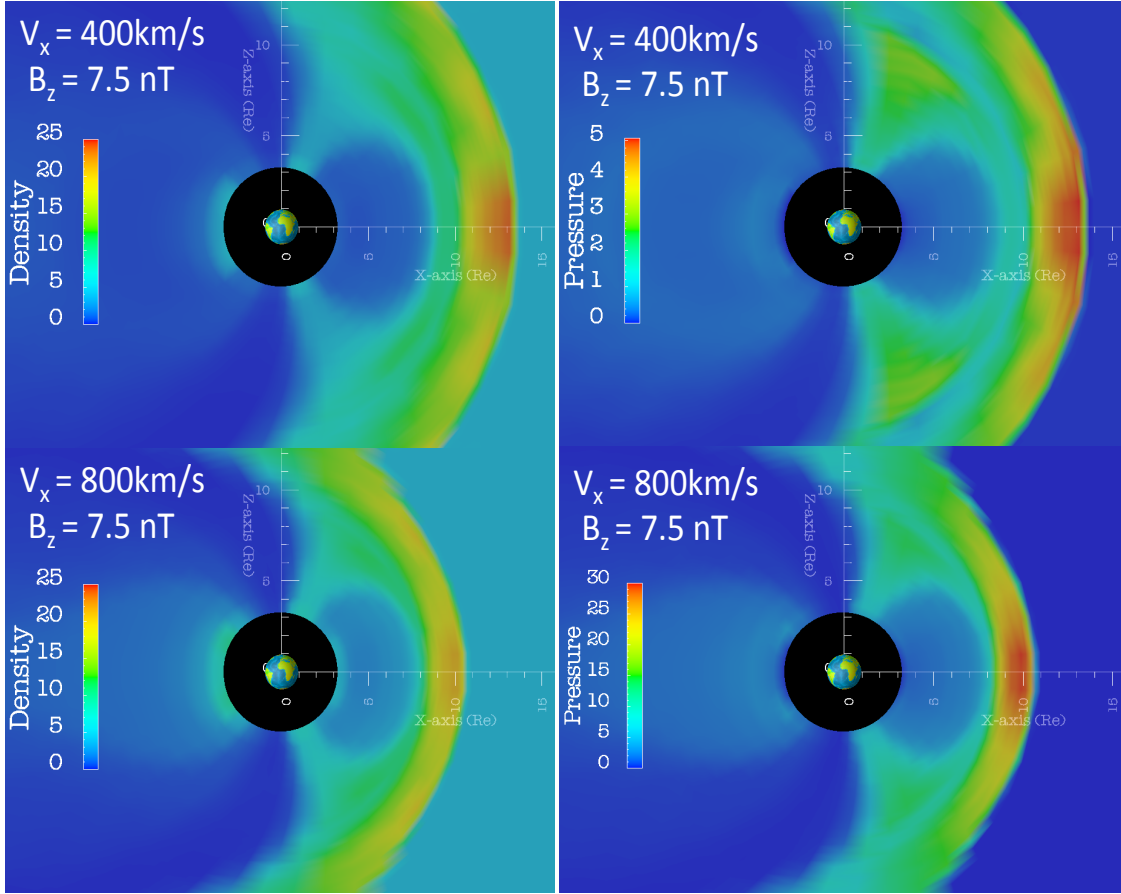
Figure 3.7. Visualization of the plasma density and pressure in the X-Z plane during cases with 7.5 nT B_z for two different solar wind velocities. Both runs have a solar wind density of 5/cc and a uniform ionospheric conductance of 10 mhos[*Bhattarai et al.*, 2012].

B_z is required to attain plasma beta equal to one (equation 3.4), thus increasing the value of B_z when saturation will occur.

Figure (3.8) shows result obtained from the LFM simulation showing plasma pressure for B_z=7.5 nT during uniform ionospheric conductivity of (a) 20 mhos and (b) 5 mhos. The solar wind speed and density were 400km/s and 5/cc respectively for both the runs. This run is well within the linear reconnection dominated regime but not close to saturation, so the effect of ionospheric conductivity on geoeffective
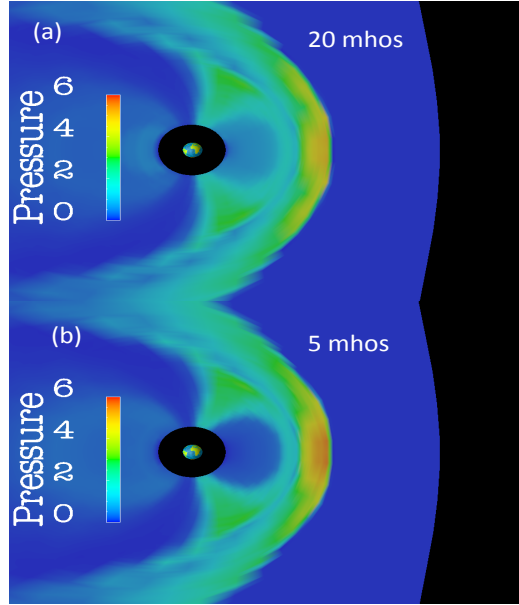
Figure 3.8. Visualization of the plasma pressure for B_z=7.5 nT during uniform iono-spheric conductivity of (a) 20 mhos and (b) 5 mhos. The solar wind speed and density are 400 km/s and 5/cc respectively for both the runs [*Bhattarai et al.*, 2012].

length can be properly understood. We know that during the northward IMF the merging occurs at higher Z-location, in the cusp region. Looking at the Figure (3.8), we see that although the pressure is higher at the nose, it is lower at higher Z for 5 mhos case compared to 20 mhos case. This implies more plasma divergence for the 20 mhos case in the post cusp region, thus decreasing the geoeffective length for higher conductivity as seen in Table (3.1).

3.4   Conclusion

During the analysis of the results obtained from the LFM simulation during periods of purely northward IMF for different solar wind velocities and ionospheric conductivities, we find a consistent behavior of variation of the CPP with the solar wind parameters as well as with the ionospheric conductivity. The CPP was seen to decrease with increasing B_z, it attains a minima beyond which the reverse convection

potential dominates the CPP value and finally saturates. We found that the viscous interaction gets weakened during periods of northward IMF, about which we will discuss in detail in chapter 4. We also found that the potential due to merging and due to viscous interaction is separable for purely northward IMF and that the reconnection potential increases with increasing B_z up to a certain value, and then saturates. Finally, we also found that the variation of the geoeffective length and the reconnection potential during northward IMF can be explained using the mangetosheath force balance model proposed by *Lopez et al.* [2010].

CHAPTER 4

VISCOUS INTERACTION DURING NORTHWARD IMF

Although a lot of work has been done to study the nature of viscous interaction (e.g. [*Burke et al.*, 1999; *Claudepierre et al.*, 2008; *Newell et al.*, 2008; *Boyle et al.*, 1997]), it is still believed that the viscous interaction is independent of the orientation and magnitude of the IMF. Whereas, in this chapter, we will show the results obtained from the LFM simulation showing that the viscous potential does depend on IMF northward B_z value, and that the viscous potential in fact decreases with increasing IMF magnitude up to a certain value, after which it asymptotically flattens. Furthermore, we also show that the magnetosphere remains mostly "closed" during purely northward IMF, except for the points where reconnection occur [*Bhattarai and Lopez*, 2013].

4.1   Viscous Interaction

As stated in Section (1.7.1), the viscous interaction occurs due to the velocity shear between the solar wind flowing close to the magnetopause and the magnetospheric plasma, producing a Kelvin-Helmholtz wave. The instability grows bigger with the square of the difference of velocities between the two fluid layers, hence producing higher viscous potential for larger velocity difference. The tailward dragging of the magnetospheric plasma by the magnetosheath plasma along the flanks produces a circulation pattern, which we call the viscous circulation pattern. This circulation pattern gets mapped on to the ionosphere via magnetic field lines, thus imposing an electric potential in the Earth's ionosphere, which is termed as the viscous potential. The viscous interaction and magnetic reconnection are completely different phe-

nomenon occurring simultaneously, but the effect of these phenomenon on the polar cap may get added up, or remain separated, depending on the orientation of the IMF. The potential imposed on the polar cap due to viscous interaction and/or magnetic reconnection has been used as an important proxy for measuring the solar wind - ionosphere coupling mechanism.
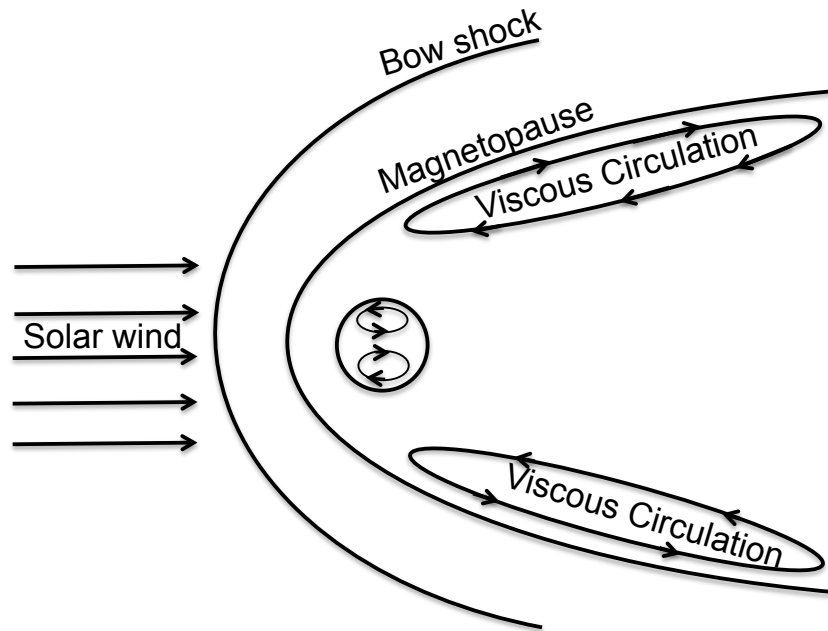
Figure 4.1. Schematic of the solar wind flow in the magnetosphere showing the generation of viscous circulation pattern. The solar wind flowing antisunward in the flanks outside the magnetopause produces circulation cells inside the magnetopause, which gets mapped to the ionosphere, thus imposing an electric field, which is measured in terms of electric potential - the viscous potential. The view is along the equatorial plane with the Sun along the left side of the page.

Figure (4.1) shows the formation of the viscous circulation pattern, and how it gets maps on to the ionosphere. The circulation pattern in the ionosphere is shown to reverse direction in this figure, because the magnetic field line originating from the inner magnetosphere maps to the lower latitude in the ionosphere, and vice versa.

There have been several previous studies to indirectly identify, as well as quantify, the viscous-driven circulation using different methods. *Reiff et al.* [1981] used AE-C and D satellite data to determine the relationship between the CPP and southward IMF condition using different coupling models, but they were unable to account for 35 ± 10 kV for all coupling functions on extrapolating the CPP versus the southward IMF plot. They suggested that this "extra" potential may be due to a viscous or "closed model" process. *Doyle and Burke* [1983] also found a residual CPP of about 40 kV on analyzing S3-2 satellite data, and further found that this value drops to 20 kV after the relaxation of CPP as seen by *Wygant et al.* [1983]. *Boyle et al.* [1997] studied the relationship between steady solar wind conditions and the CPP, and found that as the IMF tends to zero, a small residual potential still remains on the system and this potential varies as $10^{-4}V^2$, where V is the solar wind velocity in km/s. *Burke et al.* [1999] analyzed the data obtained from the DMSP (Defense Meteorological Satellite Program) satellites as well as the S3-2 satellite data and found the viscous potential to be 32.6 and 34.4 kV respectively. *Shepherd et al.* [2003] found an unaccounted potential of 17 kV on analyzing the SuperDARN (Super Dual Auroral Network Data) data while fitting these data on to the Hill model ([*Siscoe et al.*, 2002a]). *Newell et al.* [2008] performed fits of different magnetospheric parameters and proposed a formula that best fits the data to account for viscous interaction. He proposed $n^{1/2}V^2$ as the scaling factor, where n is the number density (in cm^{-3}) and V is the magnitude of solar wind velocity (in km/s).

The in-situ measurement of the viscous interaction is very improbable at present because, first of all, it is very rare to find a solar wind period where the IMF is close to zero and for which the density and velocity are not fluctuating for an extended period of time. Secondly, even if we find a period like this, it is very unlikely that the satellites will be at the right place at the right time to determine the ionospheric

potential. Thus the simulation of the geospace system would be an ideal approach to deal with this problem, and moreover, we can also run simulations with desired solar wind condition, including the case where the total IMF is zero. A simulation result with a zero IMF case would be an ideal approach to enhance the understanding of the viscous interaction in the geospace, from which we can determine the "ground state" in order to discuss about the viscous contribution of the solar wind during finite IMF cases. *Sonnerup et al.* [2001] performed simulations for zero IMF using the Integrated Space Weather Model (ISM) and found a narrow and stretched region containing closed and stretchered magnetic field lines and argued this artifact may be due to the viscous interaction or mass diffusion along the flanks. They found the viscous potential of 29.9 kV for solar wind speed of 600 km/s and ionospheric conductivity of 6 mhos, which was in agreement with other observations as well. *Sonnerup et al.* [2001] proposed a formula to calculate the viscous potential as $\phi_{PC} = 3.5(V_{SW} - 185)^{0.4}$ for the velocity range of $200 \leq V_{SW} \leq 800$ km/s for a constant ionospheric conductivity of 6 mhos. They further found that the viscous potential varies with ionospheric conductivity (Σ) as $\phi_{PC} = 109.6/(8.1 + \Sigma_P)^{1/2}$. *Bruntz et al.* [2012a] used the LFM simulation model to perform an extensive study on the variation of the viscous potential value for different values of solar wind speed and density at an ionospheric conductivity of 10 mhos during steady periods, and proposed a quasi-empirical formula $\phi_V = (0.00431)n^{0.439}V^{1.33}$ kV where n is the solar wind density (in cm^{-3}) and V is the magnitude of solar wind velocity is km/s. This proposed formula has also been found to be in good agreement with results obtained from the LFM simulation when the simulation was driven by a real solar wind, and hence was not steady [*Bruntz et al.*, 2012b].

In the upcoming section, we will discuss about the results obtained from the LFM simulation during periods of purely northward IMF and argue how and why the viscous potential gets reduced during northward IMF.

4.2 Reduction of the viscous potential in the LFM simulation

The reduction of the viscous potential observed during the LFM simulation can been analyzed both from the ionsopheric as well as magnetospheric aspect. The dynamics occurring in the magnetosphere due to the viscous interaction gets mapped to the ionosphere, the effect of which can also be observed in the ionosphere.

4.2.1 Ionospheric Aspect of Reduction in Viscous Potential

The viscous interaction occurring along the flanks of the magnetosphere gets mapped into the ionosphere via magnetic field lines. This interaction is measured in the ionosphere in term of electric potential which is called the viscous potential (VP). Similarly, the potential imposed in the ionosphere due to magnetic reconnection is called the reconnection potential (RP). Depending on the orientation of the IMF, the overall geometry of the mapping of these potentials onto the ionosphere varies. When the IMF is purely southward, the potential imposed in the ionosphere due to viscous as well as reconnection cycle overlap forming a two cell convection pattern (e.g. [*Dungey*, 1961; *Lopez et al.*, 2010]). If the IMF is purely east/westward, then a typical three cell convection pattern in seen in the ionosphere (e.g [*Mitchell et al.*, 2010; *Rich and Hairston*, 1994]).

For purely northward IMF a typical four cell convection pattern is formed which has been observed in situ as well as in simulation by various authors (e.g. [*Burke et al.*, 1979; *Crooker*, 1992; *Cumnock et al.*, 1995; *Huang et al.*, 2000; *Bhattarai et al.*, 2012]). The details of the geometry of a four cell convection pattern and its significance in

46

determining the viscous contribution during purely northward IMF has already been discussed in Section (3.2).
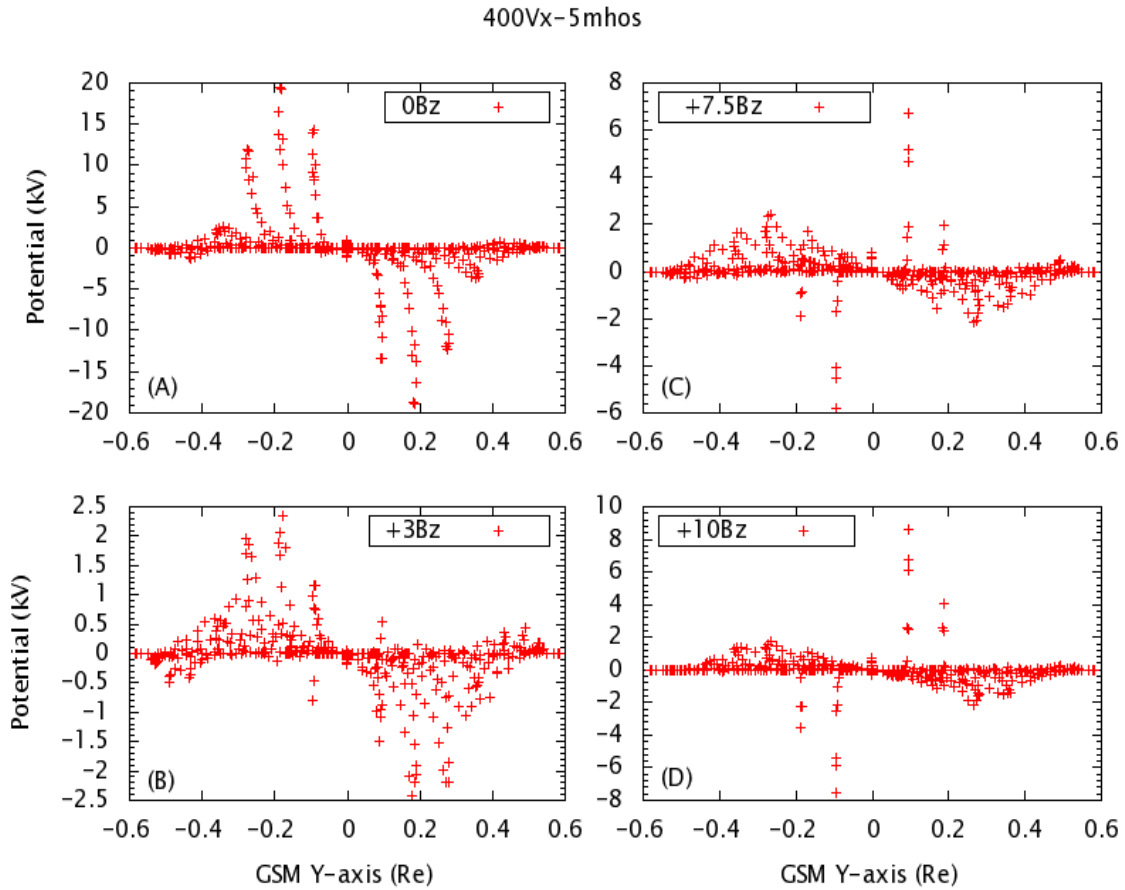
Figure 4.2. Plots showing the distribution of the ionospheric potential in the northern hemisphere from dawn to dusk (the Y axis in the ionosphere) as seen in the LFM simulation for (A) 0, (B) +3, (C) +7.5, and (D) +10 nT B_z. The data points are the values of the ionospheric potential for all values of X (the Earth-Sun line) at a given Y value. All these plots correspond to solar wind velocity and density of 400 km/s and 5/cm^3 respectively, with an ionospheric conductivity of 5 mhos. The X-axis corresponds to the dawn-dusk line and the Y-axis is the value of the potential at the corresponding coordinates..

Figure (4.2) shows the distribution of the ionospheric potential as seen in the LFM simulation on the northern hemisphere as viewed from the Sun for (A) 0, (B)

+3, (C) +7.5, and (D) +10 nT B_z. Each data points corresponds to a unique grid point in the ionosphere for a given simulation run and fix for a given fixed time step. The data points are the ionospheric potential values for all values of X (the Earth Sun line) at a given Y value. All the plots are for solar wind speed and density of 400 km/s and 5/cm^3 respectively, and the ionospheric conductivity was fixed at 5 mhos. Figure (4.2) (A) represents a typical two cell convection pattern (similar to Figure (3.1)(A)) in the ionosphere during zero IMF condition, and the CPP value obtained in this case (40 kV) is the viscous potential value for the solar wind condition specified above.

Now, as the northward IMF gets stronger, two important features are observed in Figure (4.2) (B), (C) and (D). Firstly, a reverse potential begin to appear closer to the pole in the lower IMF values and this reverse potential starts getting stronger with increasing IMF magnitude. This reverse potential must be due to the magnetic reconnection occurring at higher latitude during northward IMF causing a sunward flow, which generates a potential whose orientation is opposite to the viscous potential. Thus, the reverse convection potential is seen to get stronger, numerically as well as spatially, with increasing northward IMF value. Secondly, the magnitude of the viscous potential is observed to decrease with increasing IMF magnitude. When the IMF increases from 0 to 3 nT B_z, the viscous potential is seen to drop from 40 kV to about 5 kV, thus suggesting a reduction in viscous potential for northward IMF.

Figure (4.3) shows the decrease in the viscous potential with increasing IMF magnitude during northward IMF at different solar wind speeds of 400, 600 and 800 km/s, solar wind density of 5/cm^3, and an ionosphere conductivities of (A) 5 and (B) 10 mhos. The viscous potential is seen to decrease sharply when B_z increases from 0 to 3 nT. *Sundberg et al.* [2009b] did an analysis to determine the boundary layer potential during periods of strong northward IMF and determined the boundary layer
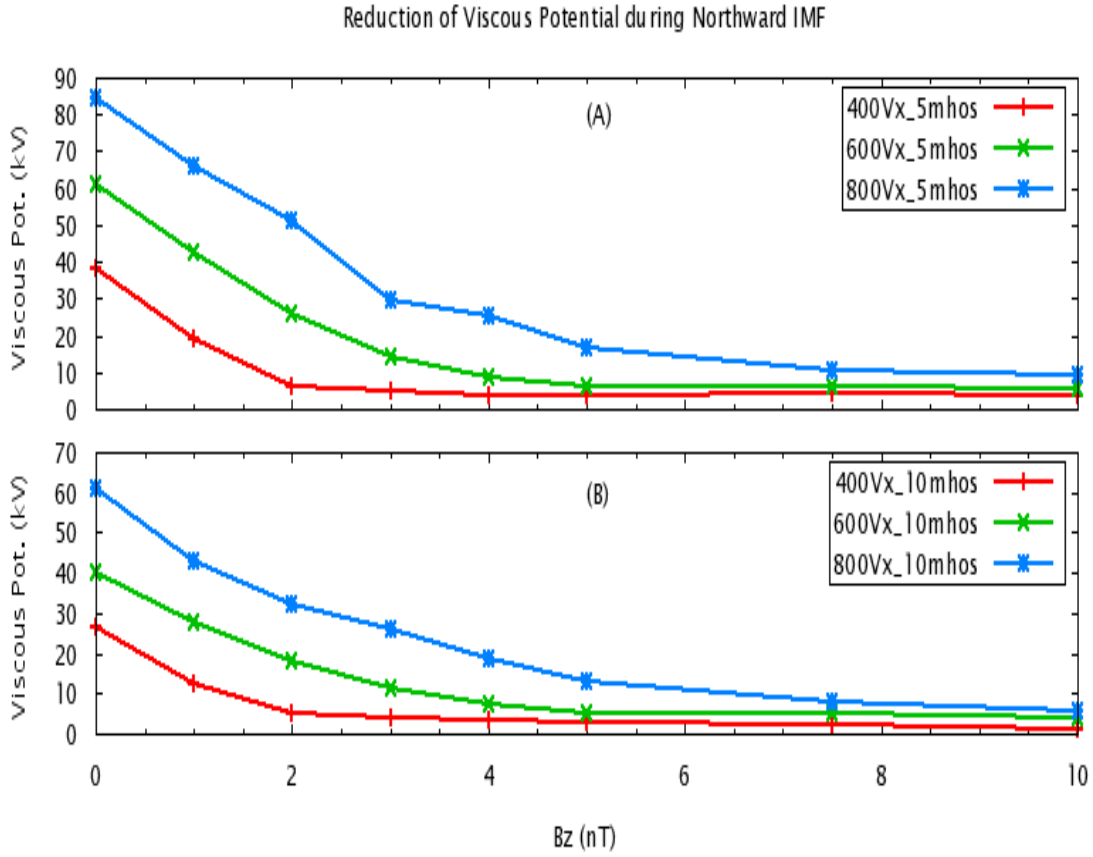
Figure 4.3. Plots showing the reduction of viscous potential for northward IMF for two different ionospheric Pedersen conductivities of (A) 5 mhos and (B) 10 mhos. The results correspond to the solar wind density and velocities of 5/cm³, and 400, 600 and 800 km/s respectively.

potential of about 10 kV on analyzing 271 DMSP F-13 satellite passes. They also found that the boundary layer potential depends on the viscous parameters such as solar wind speed, density and ram pressure.

4.2.2 Magnetospheric Aspect of Reduction in Viscous Potential

As stated earlier, the generation of the viscous interaction starts at the magnetospheric flanks and gets mapped on to the ionosphere via magnetic field line. Thus,

it is important to understand the dynamics occurring in the magnetosphere that produces the viscous circulation pattern. The antisunward dragging of the plasma in the low latitude boundary layer (LLBL), followed by a sunward flow deeper inside the magnetosphere is what causes the viscous circulation. The LLBL can be defined as the region between the magnetopause boundary (or the open-closed field line boundary) and the flow reversal boundary in the magnetosphere.
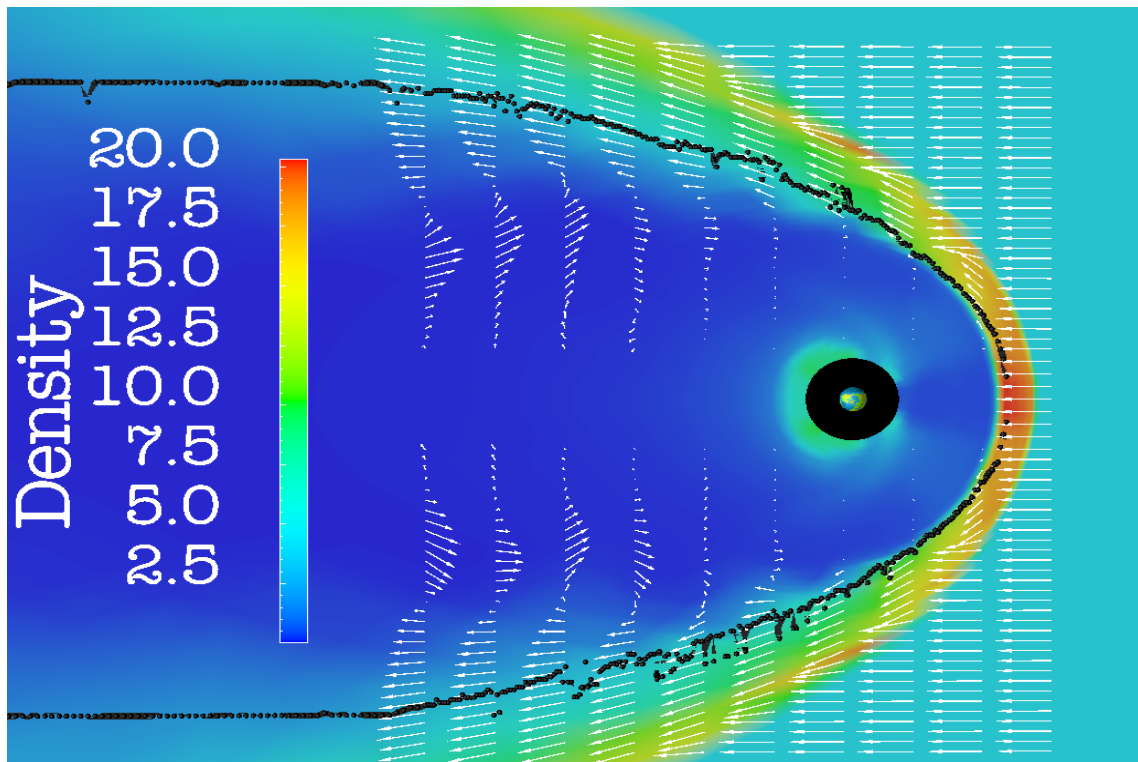
Figure 4.4. Result obtained from LFM simulation showing the formation of viscous circulation pattern in the magnetosheath in X-Y plane. The simulation was run with solar wind density of 5/cc, velocity of 400km/sec, null IMF and at an ionospheric conductivity of 5 mhos. The white arrows represent in magnitude and direction, the solar wind velocity along the X-Y plane. The black countour represents the open-close field line boundary. The Sun is on the right side of the page.

Figure (4.4) shows the result obtained from the LFM simulation showing the magnetospheric X-Y plane during the solar wind density, velocity and IMF of $5/cm^3$, 400 km/s and 0 B_{tot} respectively with ionospheric conductivity of 5 mhos. As the simulation has been run with 0 B total (i.e. no magnetic field) there is no magnetic reconnection, implying all plasma flow along the tail should be due to the viscous interaction. The Sun is on the right side of the figure and the white arrow represents in magnitude and direction, the plasma flow velocity at those points. The black contour represents the open-closed field line boundary - a good proxy for the magnetopause location during northward IMF cases. The open-closed field line boundary for all the simulation results henceforth has been determined by locating the last closed field line along GSM Y-axis on both the flanks for a given GSM X-value.

In this figure we see that in the magnetosheath, the plasma is flowing antisunward but as we enter inside the magnetopause, the plasma velocity starts to decrease, and finally turns sunward. As this image corresponds to 0 B total implying no magnetic reconnection, it clearly shows the existence of a convection pattern along the flanks which must have been due to viscous interaction. The existence of viscous convection cells in LFM simulation has also been shown in detail by *Bruntz et al.* [2012a], where they have shown that this pattern gets stronger as the solar wind speed or density increases - a typical characteristic of viscous interaction found from the real solar wind data analysis by different authors. [*Newell et al.*, 2008] investigated satellite data and came out with an empirical formula to calculate the viscous coupling for a given solar wind condition where they show that the viscous coupling is proportional to the square of the solar wind velocity. Also, *Bruntz et al.* [2012a] have come out with an simulation based "empirical" formula to calculate viscous potential in the LFM simulation for a given solar wind condition and these models have been shown to match each other after introducing an appropriate scaling factor.
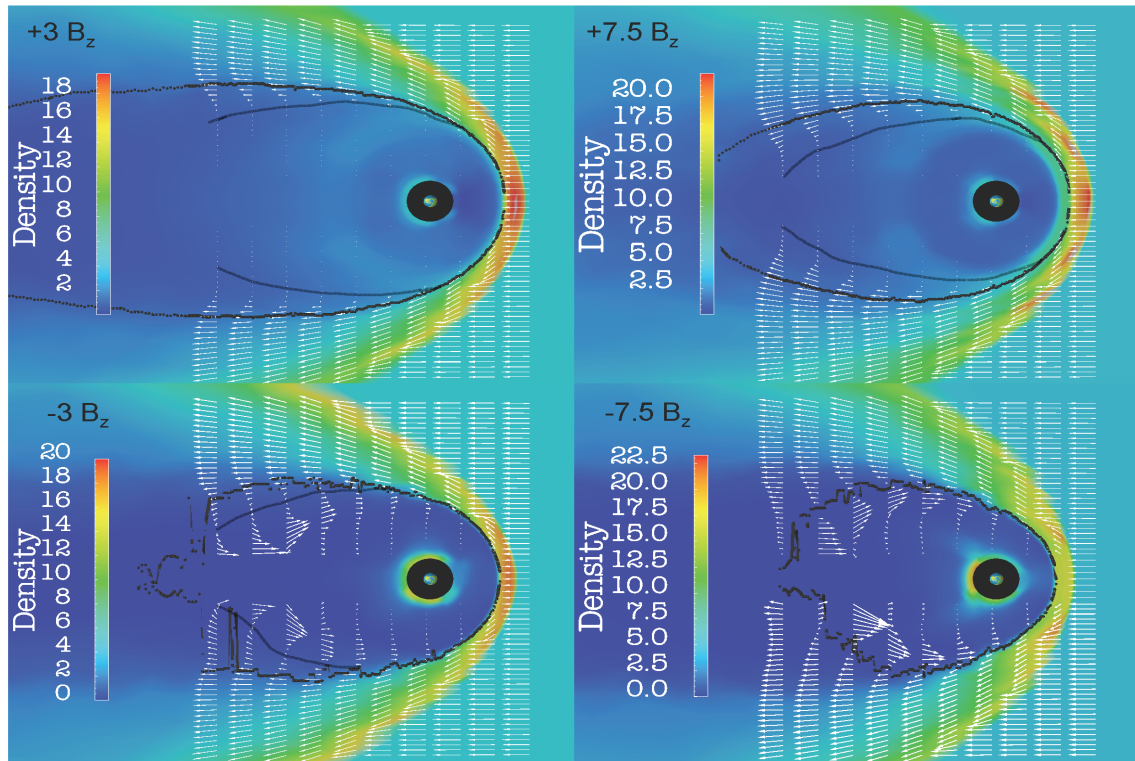
Figure 4.5. Plots obtained from the LFM simulation showing velocity distribution in the magnetosphere for ± 3 and ± 7.5 B_z. The solar wind velocity and density are 400 km/s and 5/cm^3 respectively and the ionospheric Pedersen conductivity was set to 5 mhos. The white arrows depicts the plasma velocity, in both magnitude and direction, a the base of the arrow. The outer black contour represents the open-closed field line boundary and the inner black line represents the flow reversal boundary. The region between these two black lines is the low latitude boundary layer. The view is of the GSM X-Y plane as seen from above the north pole with the Sun on the right side of the page.

Figure (4.5) shows result obtained from the LFM simulation, which compares the plasma flow pattern for the IMF values of ± 3 and ± 7.5 nT in the GSM X-Y plane color coded by density, with the Sun at the right side of the page. The outer black contour represents the open-close field line boundary, whereas the inner black line is the flow reversal boundary. All figures are obtained for the case where the solar wind speed and density was 400 km/s and 5/cm^3 respectively, and the ionospheric conductivity was set to 5 mhos. If we compare the plasma flow between the +3 and
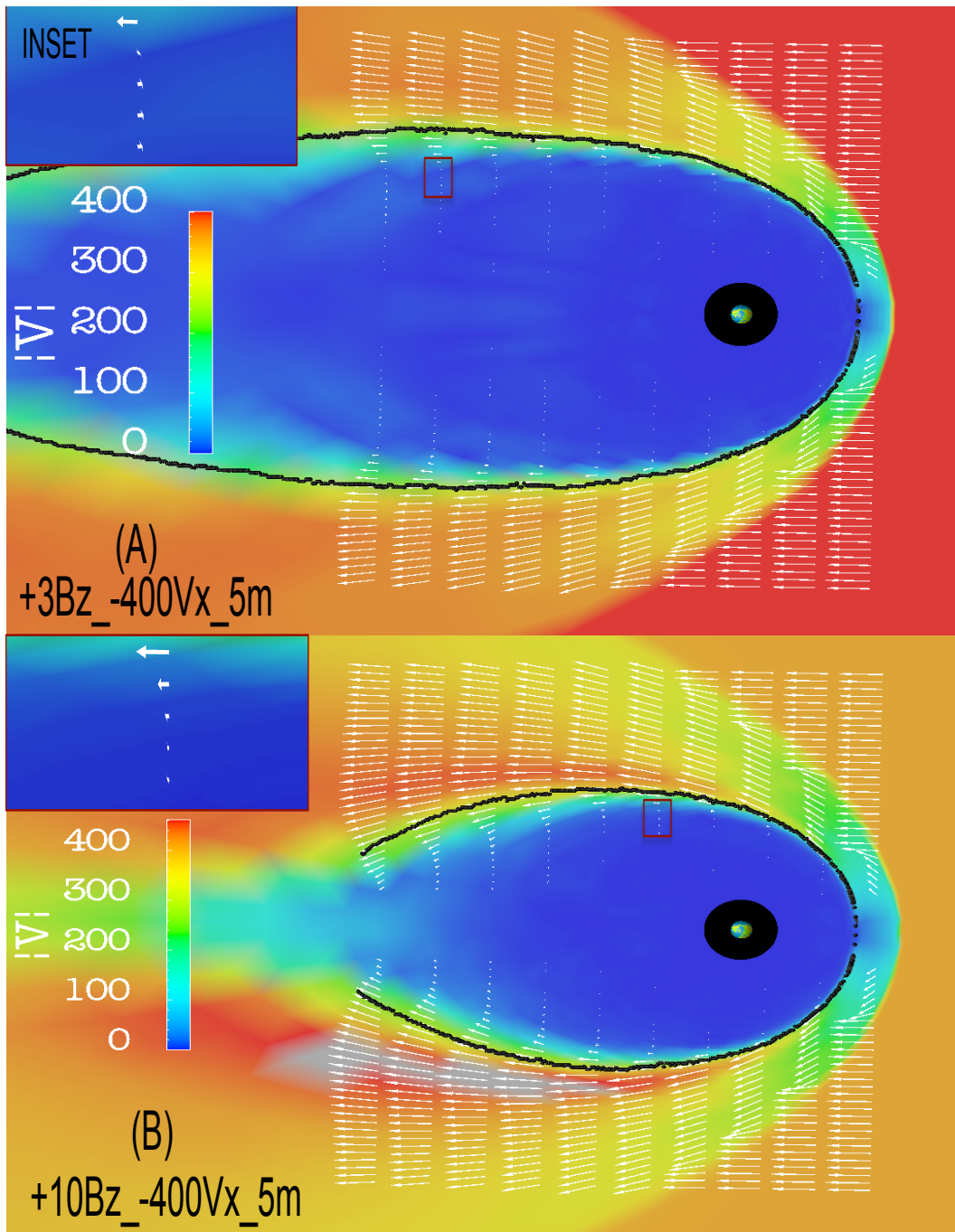
Figure 4.6. The flow vectors in the magnetosphere in the equatorial plane during (A) B_z of +3 and (B) +10 nT respectively for solar wind speed and density of 400 km/s and 5/cm^3 and an ionospheric conductivity of 5 mhos. The black line represent the open-closed field line boundary and the inset shows a zoom-in of the section enclosed by a brown rectangle in the main figure. The color coding shows the velocity magnitude.

-3 B_z, we clearly see a strong sunward flow in the magnetosphere for the southward IMF case, whereas the reverse flow in the +3 B_z case is very weak. Similar result is seen when we compare the figure for + 7.5 and -7.5 nT B_z runs. Furthermore, a close comparison of the plasma flow pattern between +3 and +7.5 nT B_z shows a weak sunward flow for the +3 nT Bz case, whereas the sunward flow seems to be non-existent in the +7.5 nT B_z case, which implies that the viscous potential is reduced during higher northward IMF value due to the lack of a return flow. Whereas when we compare the flow pattern for -3 and -7.5 nT case, the return flow is seen to be stronger for higher southward IMF value, which is consistent with the Dungey -type circulation driven by reconnection.

Figure (4.6) shows in detail about the flow pattern in the magnetosphere that would occur for two different northward IMF values of 3 and 10 nT B_z. This figure shows the GSM X-Y plane color coded with total flow speed, with the Sun at right side of the page. Both the images correspond to the simulation result for solar wind speed and density of 400 km/s and 5/cm^3, where the ionospheric conductivity was set to 5 mhos. The white line depicts the plasma flow vector and the black contour represent the open-closed field line boundary. The "INSET" part shows the zoom-in version of the small brown rectangle drawn in the magnetosphere for each image. In this figure, the flow pattern in the "INSET"s implies that there exist a very weak sunward flow in the magnetosphere when the IMF is +3 nT, but as the IMF magnitude increases to +10 nT, the return flow can not be detected. This lack of return flow is what causes the decrease in viscous potential.

During northward IMF, we know that the magnetic reconnection occur pole-ward of the cusp region between a closed-lobe field line and the IMF, thus producing an "IMF-type" field line that gets carried tailward, and a closed field line that moves sunward. This sunward motion of the closed field line causes plasma to accumulate

54

on the noon region on the closed field lines in the magnetosphere. This closed field line that moved sunward gets carried away towards the nightside, thus producing an antisunward flow inside the magnetopause, hence reducing the viscous interaction. *Li et al.* [2005] analyzed the OpenGGCM model to study the plasma sheet formation during periods of long northward IMF, where they demonstrated the magnetic field circulation pattern for northward IMF. Their model showed the magnetic reconnection occurring between the lobe field lines and the IMF in the cusp region, thus slowing down the tailward flow of plasma and producing a sunward flow. They further show (in Figure 3 of *Li et al.* [2005]) how a newly formed closed field line on the day side convects to the nightside within the magnetopause. This tailward motion of the plasma in a closed field line decreases the velocity shear between the boundary plasma layers, thus decreasing the viscous interaction.

Figure (4.7) shows the plasma pressure distribution in the equatorial plane color coded with pressure, as seen in the LFM simulation for IMF values of +3 and +10 nT B_z. The white arrow represents the plasma flow vector and the black contour represents the open-closed field line boundary. As we can see from the figure, the plasma flows towards the nightside parallel to the open-closed field line boundary and that the LLBL during 10 nT is larger than that of 3 nT. This larger LLBL for higher Bz value has a stronger tailward flow inside the magnetopause due to higher rate of reconnection for stronger B_z. Furthermore, the second "IMF-type" field line produced during magnetic reconnection is carried down the tail by solar wind momentum, and thus does not get involved with dynamics in the magnetopshere. Hence, the formation of thicker LLBL with stronger tailward plasma flow inside for a higher value of B_z explains why the viscous potential gets reduced with increasing northward IMF magnitude.
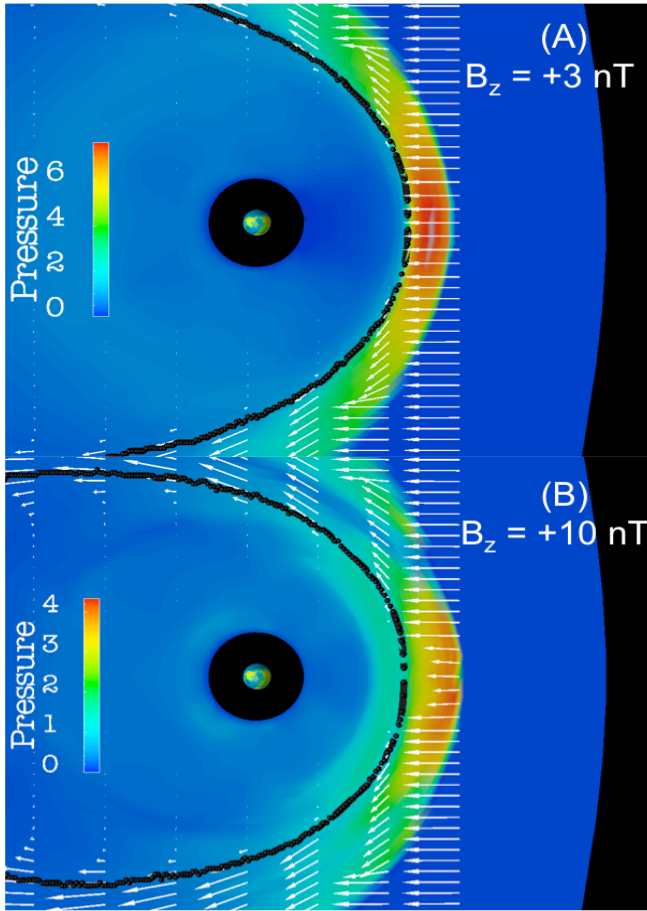
Figure 4.7. The velocity distribution (white arrows) in the equatorial plane as seen in the LFM simulation during IMF values of (A) +3 nT and (B) +10 nT respectively, with the solar wind speed and density being 400 km/s and $5/cm^3$. The plane has been color coded with pressure (keV/cm^3). The black lines represents the open-closed field line boundary.

4.3 A Closed Magnetosphere during Northward IMF

As stated earlier, the viscous interaction gets mapped to the ionosphere via magnetic field lines. The LFM simulation also maps the magnetic field lines in to the 3 R_E boundary, below which it is mapped directly in to the ionosphere. Thus we can always reverse this procedure and study how the magnetic field lines would look like corresponding to the seed points located in the ionosphere. Thus using data obtained to plot Figure (4.2), which shows the location in the ionosphere where the viscous or
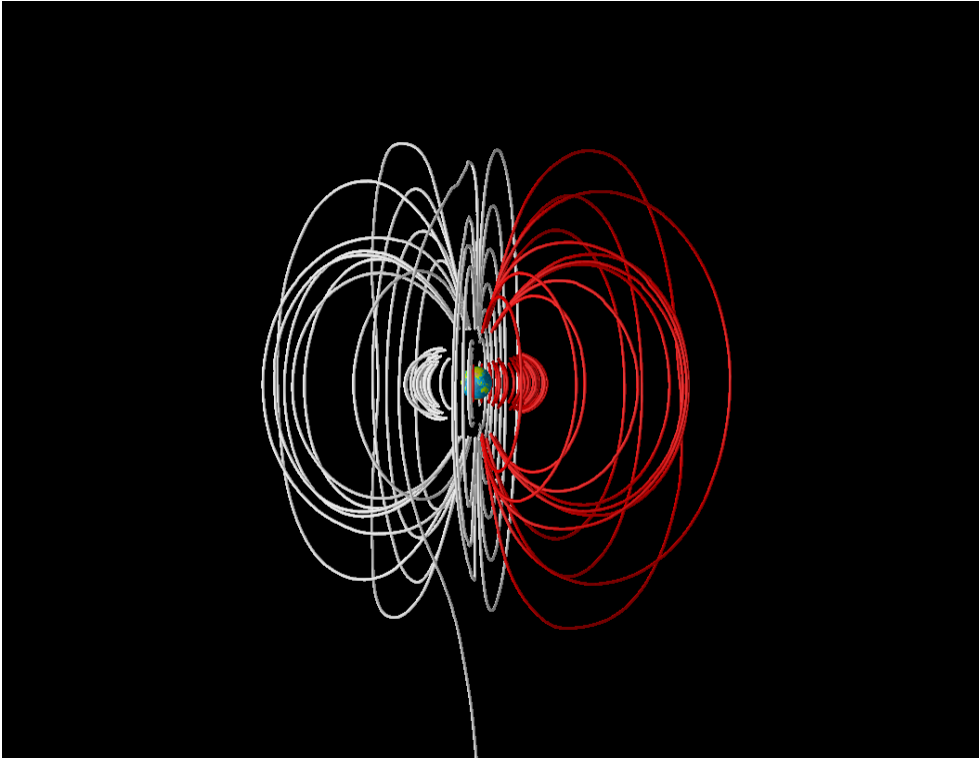
Figure 4.8. The overall magnetic field line configuration as seen in the LFM simulation for +10 nT. The footpoints of these magnetic field lines originate from the ionosphere and correspond to the coordinates that generated the four cell convection pattern in Figure 4.2(D). The solar wind velocity and density were 400 km/s and 5/cm^3 respectively and the ionospheric Pedersen conductivity was set to 5 mhos. The view is from the Sun, toward the Earth. The white and red lines correspond to magnetic field lines originating from the dawn and the dusk side respectively.

the reverse convection cell map to, the magnetospheric field line distribution looks like Figure (4.8).

Figure (4.8) shows the magnetic field line distribution as seen in the LFM simulation for +10 nT B$_z$. The foot points of these magnetic field are at the ionosphere and are the set of coordinates that corresponds to the four cell convection pattern in Figure (4.2)(D). The solar wind velocity and density was fixed at 400 km/s and 5/cm^3, and the ionospheric conductivity was set to 5 mhos. The view is along the Sun Earth line, with Sun located outside the page. The white and the red field

lines represent the magnetic field lines originating from the dawn and the dusk side respectively. Although it was expected that the magnetic field lines originating from coordinates corresponding to reverse convection cell would produce a open field line, this was not observed for any of the northward IMF case. This figure here shows that except for one field line which is open, the entire magnetosphere is closed during purely northward IMF. The closed magnetosphere during purely northward IMF was also seen by *Song et al.* [2000] in the simulation, where they argue that for except for the point where the reconnection occur, the magnetosphere is entirely closed.

4.4   Conclusion

The LFM simulation thus shows the reduction of the viscous potential during purely northward IMF. The viscous potential is seen to decrease sharply from 0 to 3 nT B_z after which the potential is seen to settle asymptotically to a smaller value. The closed field line formed in the dayside due to magnetic reconnection in the cusp region convects towards the night side, thus creating a antisunward flow in the LLBL. The antisunward flow present in the LLBL causes the reduction of velocity shear between the magnetosheath and LLBL plasma, thus reducing the viscous interaction. The decrease in visous potential with increasing IMF value was found to be due to piling of the plasma in the magnetosheath, as well as in the closed field lines on the noon side, due to high latitude reconnection. This pile of plasma moves antisunward along with the closed magnetic field line, thus producing a stronger tailward flow in the LLBL, hence reducing the velocity shear across the magnetopause and thus reducing viscous potential for higher B_z values. It was also found that except for a small region where the magnetic reconnection occur, the rest of the magnetosphere is closed.

CHAPTER 5

THE LFM SIMULATION DURING THE WHOLE HELIOSPHERE INTERVAL

5.1   Introduction

The whole heliosphere interval (WHI) refers to a single Carrington rotation (2068), which started March 20 - April 16, 2008 corresponding to the day of year (DOY) 80 -107 [*Lopez et al.*, 2012; *Bruntz et al.*, 2012b]. In this chapter we will talk about the results obtained from LFM and the coupled magnetosphere ionosphere thermosphere (CMIT) simulation model when they were run with a real solar wind over the WHI, and compare/contrast our results with the other models and observational data.

Figure (5.1) shows the solar wind density, speed, and B_y and B_z component of the IMF during the WHI obtained from the OMNI data. OMNI is a database that collects solar wind data from different satellite and predicts the solar wind parameters at the edge of the bowshock. The corotating interaction regions (CIRs) have been shaded blue and the high speed streams (HSS) interval has been shaded yellow, with some dark patches implying that the CIR accompanied the HSS. The WHI corresponding to Carrington rotation 2068 consist of two CIRs followed by the HSS.

During solar maximum, the geospace environment is driven by numerous coronal mass ejections (CMEs), whereas during solar minima there is a prevalence of coronal holes and CIRs. The CIRs are formed due to the combined effect of solar rotation and variation in the solar wind speed, which causes high speed streams to overtake slower streams. The solar wind is considered a HSS if the daily average
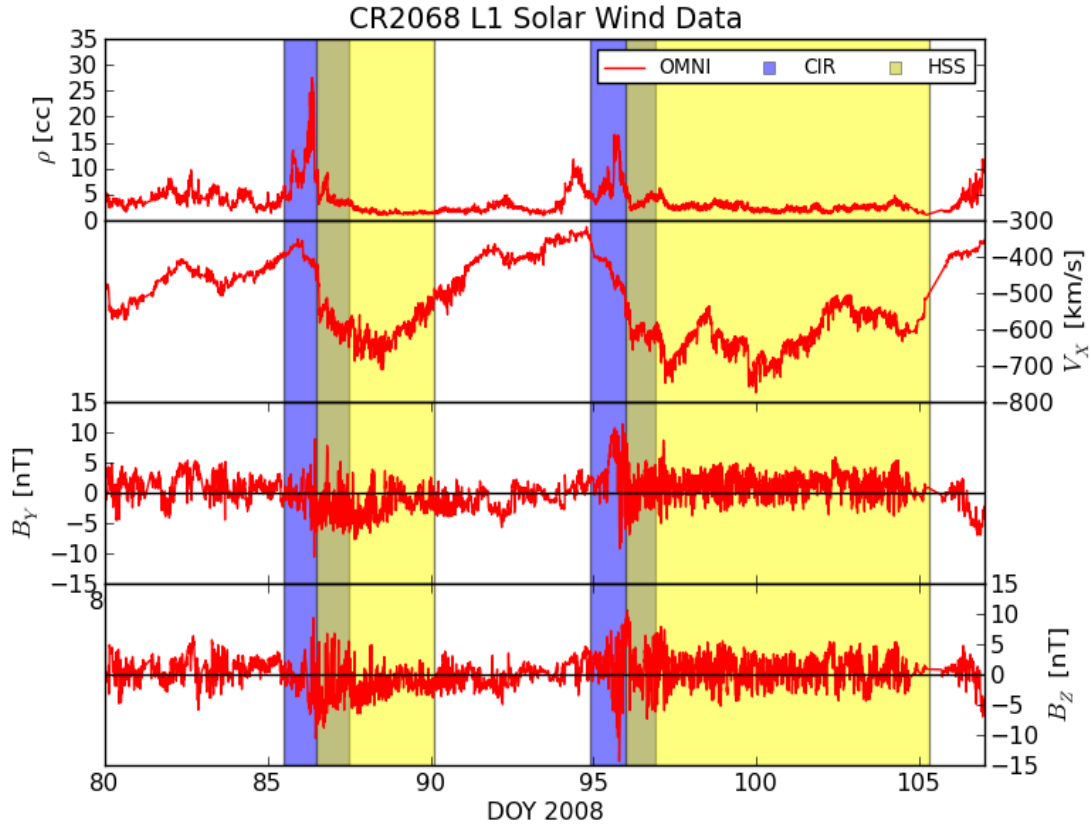
Figure 5.1. Plot showing the density, velocity, B_y and B_z component of the solar wind during the WHI. The blue and the yellow shaded region correspond to the CIRs and the HSS respectively.

speed of the solar wind is $\geq$ 500km/s [*Broussard et al.*, 1978]. We will use the results obtained from the CMIT model, along with results from other models, to compare it with the stand-alone LFM simulation during the WHI. In our stand-alone LFM version, we used the F10.7 flux of 74 SFU (solar flux unit), which was the average F10.7 value over the WHI.

5.2   The merging potential during southward IMF

Figure (5.2) compares the CPP obtained from the CMIT model and the stand alone LFM model (Chapter 2) with the CPP obtained from the LFM model when the IMF value was set to zero. The results from CMIT run, the LFM run and the LFM run without IMF are shown in red, black and blue color respectively.
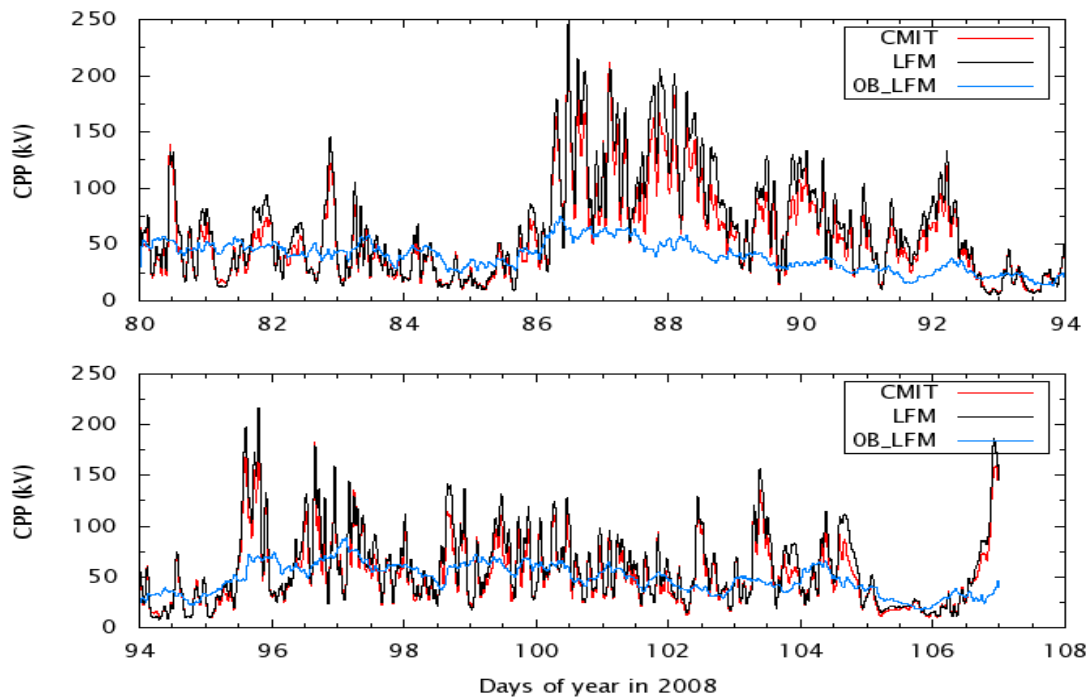
Figure 5.2. Plot comparing the CPP obtained from CMIT (red), the stand-alone LFM (black), and the stand-alone LFM with the IMF set to Zero(blue).

In the CMIT model, the magnetosphere uses the LFM simulation model and the ionosphere-thermosphere regime is modeled using the thermosphere-ionosphere-electrodynamics general circulation model (TIE-GCM) [*Richmond et al.*, 1992]. The TIE-GCM solves the 3D momentum, energy and continuity equations for the ion and neutral species. The F10.7 solar index is most widely used as the solar input to

TIE-GCM, and the IMF condition is used as an input to determine the high-latitude electric fields for the Weimer convection model. It outputs the height of the pressure surfaces, temperatures, composition and density of the ions and neutral species.

From Figure (5.2) we can see that the CPP obtained from the CMIT model and the stand-alone LFM model are very close to each other, although the LFM tend to estimate higher values than the CMIT particularly at peak times. The LFM has been known to produce higher potential during southward IMF as compared to observation [*Merkin et al.*, 2003; *Lopez et al.*, 2009] due to the insufficient ionospheric criteria on the model. The CPP obtained from the stand-alone LFM with B =0 nT run during the WHI represents the contribution of the viscous interaction over that period. We applied a Hanning filter with 90 min window to the CPP obtained from stand alone LFM as well as the LFM run with zero IMF (will be referred hereon as 0 B run) in order to smoothen it. A simulation with 0 B causes a lack of pressure balance in the magnetosphere but as the flow is super Alfvénic, any inconsistency would not be dynamically important. All the LFM runs have been time shifted in order to take into an account the initialization period required for the LFM runs.

Lopez et al. [2010] applied two different methods to calculate the reconnection potential during southward IMF. In the first method, he used the value of the viscous potential obtained during a steady state solar wind condition and subtracted it from the CPP to calculate the contribution due to magnetic reconnection. Thus, this value of the reconnection potential is obtained from the ionospheric data which is purely driven by the Birkeland current in the LFM simulation. For the second method, he utilized a magnetospheric approach where he calculated the rate magnetosheath flow that reaches the merging line. He found that the rate of flux transport was the same as the CPP minus the viscous potential value, validating that the calculation of merging rate in the magnetosphere also gives us the merging rate. Thus, as the total

CPP during southward IMF is the sum of the viscous and the reconnection potential, we can obtain the reconnection potential during the WHI by subtracting the viscous contribution obtained from 0 B runs [*Bruntz et al.*, 2012a] whereas during northward IMF, the viscous and the reconnection region are separate [*Bhattarai et al.*, 2012], as discussed in Figure (3.2).

Figure (5.3) shows two days of the WHI and has a mixture of northward as well as southward IMF. The top panel in each figure represents the difference of the CPP and the viscous potential obtained from 0 B runs whereas the bottom panel shows the IMF Bz component during that time. We can see from this figure that as the Bz turns northward the reconnection potential attains a negative value suggesting the viscous potential being higher than the CPP during those periods. This correlation is although not perfect for northward IMF and would not work if the reconnection potential is higher that the viscous potential, which occur during high Bz values. We also see that there are occasional, short-duration IMF B_Z reversal not followed by the reversal of the reconnection potential. Although the ionosphere responds quickly to the orientation of the convection cells, it takes some time (15-20 min) for the system to produce the full potential associated with the new Bz value and dying away of the Birkeland currents [*Lopez et al.*, 1999]. During periods of southward IMF, the reconnection potential remains positive suggesting that the CPP is indeed the sum of viscous and the reconnection potential during southward IMF. The convection cells produced during viscous interaction is independent of IMF orientation, but during northward IMF, the reconnection cells are created in the higher latitude poleward of the cusp region. Even for very small values of northward IMF, the CPP measured is seen to be less than the viscous potential during the zero IMF condition as discussed in chapter (4).
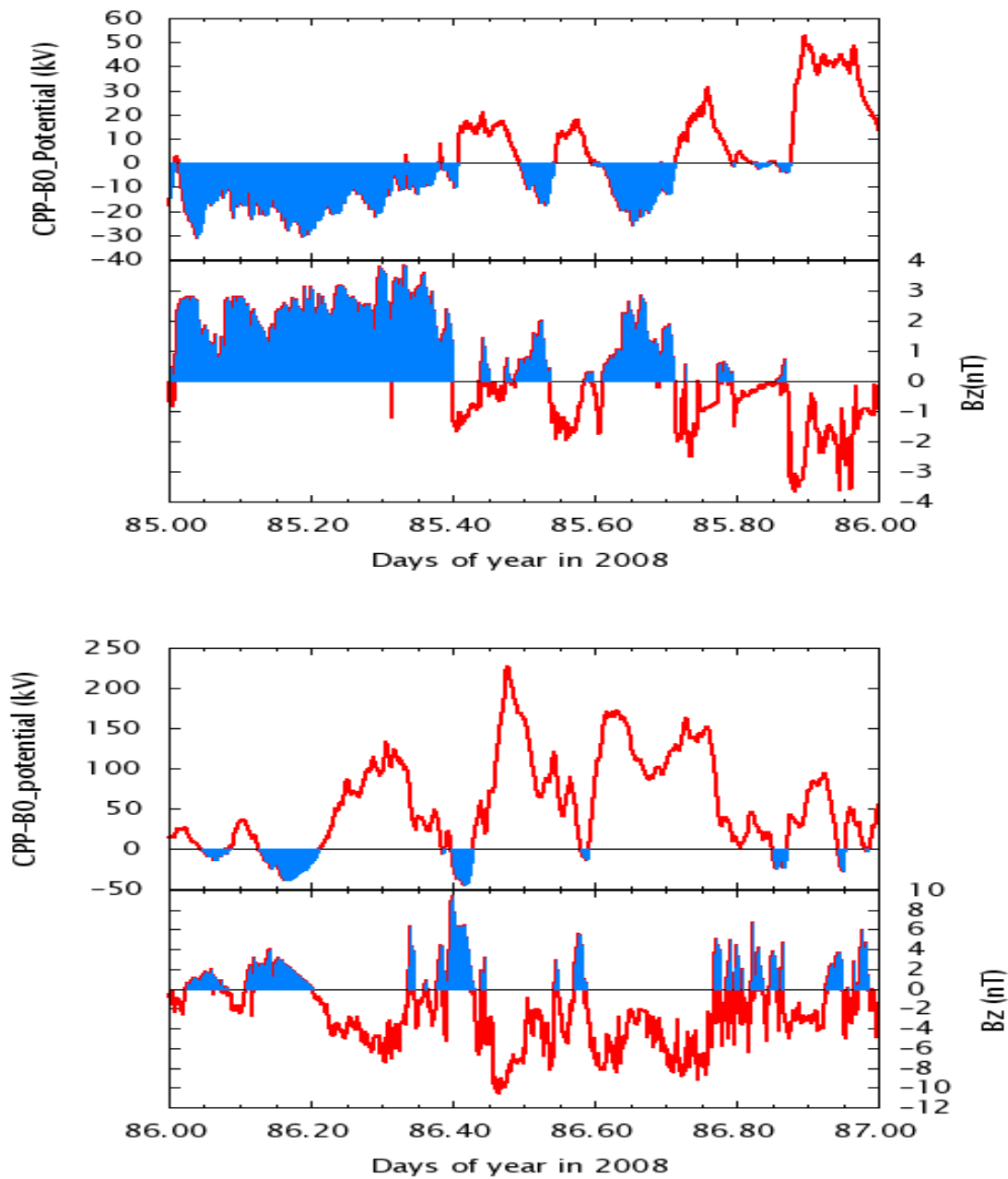
Figure 5.3. Plot showing a relationship between the reverse convection potential and the IMF Bz. We see a negative reconnection potential during periods with northward IMF.

64

5.3 Comparing viscous, merging and total potential during the WHI

The CMIT as well as the LFM run were done for the full WHI using the same solar wind input file. The CPP values obtained from LFM was interpolated to fit a 1 min cadence and was then smoothed by being run through a Hanning filter, using a 90-min window. A Hanning function performs a weighted-average of the data points with higher weight given to the data at the center. For example, for three successive inputs, with the center point of the three weighted twice as heavily as its two adjacent neighbor, the Hanning filter is performed as follows:

$$y[k] = \frac{1}{4}(x[k] + 2x[k-1] + x[k-2]) \tag{5.1}$$

This Hanning filter method was used to find the boxcar average for 1 min cadence by taking into account 90 min of data and obtain the final CPP values for the CMIT as well as the LFM runs.

All the CMIT and LFM runs has also been offset in time in order to incorporate the initialization period required to introduce the real solar wind data. This offset also had to considered to match the simulation output to the solar wind data. The offset was calculated the following way: (i) We used the Bruntz formula (equation 5.2) to calculate the viscous potential using the solar wind input (ii) we interpolated the B0 run to one minute cadence without running it through the Hanning filter and added appropriate time stamp (iii) calculated the average of the square of the difference between the Bruntz potential and the time shifted LFM B0 potential. This process was repeated for $\pm$ 100 minutes in a 10 day data and the time that yielded the lowest average of square difference was considered the offset value to be applied to the LFM runs.

$$\phi_v = 0.00431n^{0.439}V^{1.33} \tag{5.2}$$

where n is the solar wind density in /cc and V is the solar wind velocity in km/s.

As stated before, all the WHI runs were performed with a F10.7 value of 74 SFU whereas the Bruntz formula (equation 5.2) was derived from the LFM simulation when the ionospheric conductivity was set to 10 mhos. Hence we require a scaling factor in order to scale the Bruntz formula to F10.7=74 SFU condition. Due to lower conductivity produced in the ionosphere by F10.7=74 runs, the CMIT and the LFM run is seen to produce unrealistic high value of about 250 kV on day 86 with moderate B_z value. Hence, we chose to modify the Bruntz formula and scale it down. Hence we chose eleven periods the WHI where the solar wind was relatively steady and the average value of density, velocity and the CPP value for those periods were determined from which we determined the average scaling factor over all eleven events to be 1.54. Thus 1.54 is the value by which the B0 run is over-predicting the CPP.

5.4   The reconnection and the solar wind driver

We believe up to this point that the viscous potential is independent of the the IMF magnitude during southward IMF, so that subtracting the viscous from the total CPP yields the reconnection potential during southward IMF. Whereas during the northward IMF, the reconnection and viscous are already separated and hence can be determined already. Thus the effect of solar wind drivers on the reconnection potential during WHI can be studied in detail. Figure (5.4) shows the CPP minus the potential from the B0 runs (i.e. the viscous potential) as a function of VB_z for the entire WHI interval. The blue line corresponds to the condition when the reconnection potential was equal to zero and the black line represents the average reconnection minus the B0 potential found using a moving boxcar average 0.2mV/m wide. The issue of B_y dependence is not considered in a great detail here, although it plays a significant role is the formation of convection pattern due to B_y reconnection. The Figure (5.4)

has a one minute cadence along X-axis. The scattering in of the data points in this figure may be due to the ionosphere not getting enough time to return to steady state due to varying B_z and/or density and/or velocity of the solar wind. The northward IMF (E_y less than zero) the average CPP minus the B0 potential value is seen to be negative and this value for southward IMF comes to be positive. Also for southward IMF, the CPP minus the B0 potential is the reconnection potential as well, whereas for northward IMF, the CPP would either be measuring the viscous or the reverse convection potential depending on the solar wind IMF, density and velocity. For the cases when the CPP during northward IMF is measuring the viscous potential, then the CPP-B0 potential is the measure of the reduction in viscous potential, but when the reverse convection potential is measured as the total CPP, the CPP -B0 potential is does not have any meaning as it does not represent any physical process.

The average reconnection potential when $E_y=0$ is close to zero but not exactly zero. The value is found to be 14.7 kV when $E_y=0.0025$mV/m (the running average box car B_y value closest to zero). This is because the B_y component of the magnetic field also contributes to the total CPP, about which we have not worried much about in this figure as the average magnitude of B_y along WHI was about 2 nT. *Mitchell et al.* [2010] have studied the effect of pure B_y on the magnetosphere-ionosphere system and they found the CPP value of about 18 kV for 2 nT B_y, which leaves us with a reconnection potential of about 3.3 kV during north-south oriented IMF when the E_y is zero. We selected the case when the magnitude of B_y was less than 0.5 and did a moving boxcar average for those period and found that the reconnection potential during $E_y = -0.0012$mv/m (closest to zero in the data) was found to be 2.4 kV. Although the reconnection potential during zero E_y is expected to be zero, the observed discrepancy value of 0.9 kV is a remarkably small value considering (a) all the uncertainties in finding the lag between the solar wind and the CPP, (b) using a
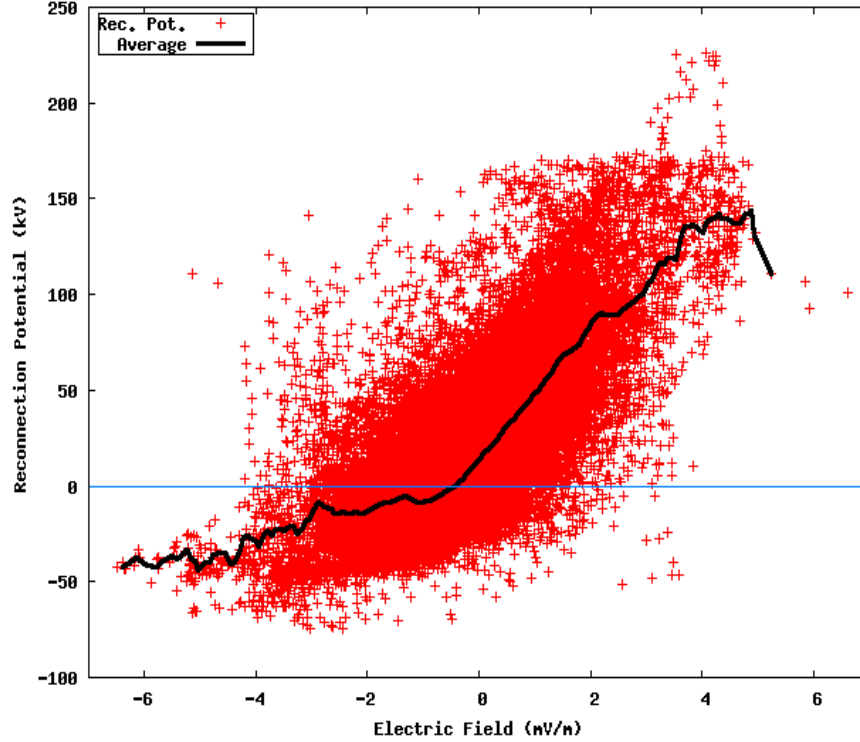
Figure 5.4. Plot showing the average reconnection potential during the WHI. The reconnection potential was obtained by subtracting the CPP and B0 potential calculated in one minute interval and plot against the solar wind E field. The black line is a sliding boxcar average 0.2mV/m wide.

single value of lag for the WHI, (c) the errors produced due to response delay in the ionosphere, (d) and the possible errors that might arise from removing the IMF from the solar wind during the B0 runs. This small discrepancy value also suggests that the subtraction of the B0 runs from the CPP during southward IMF indeed gives the reconnection potential.

The slopes of the running average in Figure (5.4) have units of length. We also see that there exists two distinct slopes corresponding to whether E_y was greater than or less than zero. For the regime where E_y is greater than zero, the slope gives us the geoeffective length (section 3.3.1). Thus for southward IMF, the geoeffective length during WHI is found to be 5 R_E. This number is comparable to the geoeffective

68

lengths determined by other authors using LFM simulation [*Lopez et al.*, 2010; *Bruntz et al.*, 2012a], though the geoeffective length is slightly lower to that those obtained for purely southward IMF conditions with uniform conductance.
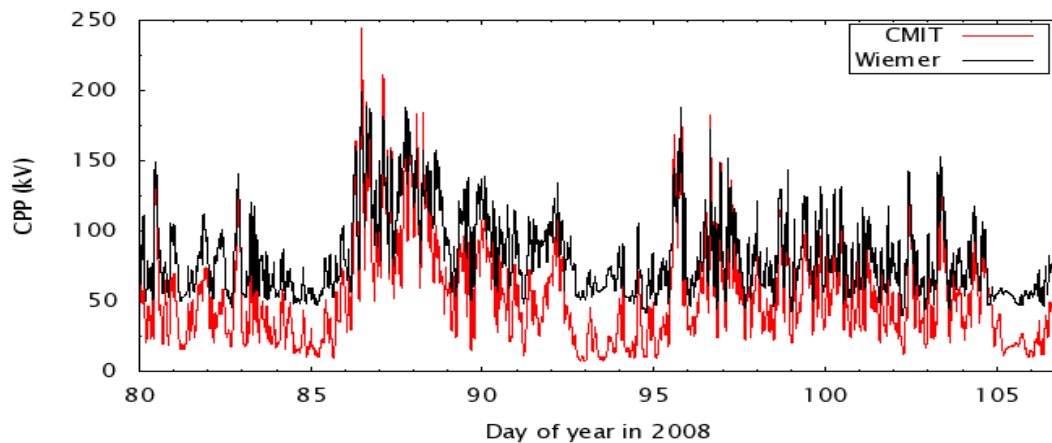
Figure 5.5. Plot showing the comparison between the CMIT CPP (red lines) and the Weimer CPP (black lines). The Weimer potential has be multiplied by a scaling factor of 1.54.

In the negative E_y regime the slope of the line is about 2 R_E, but this value does not represent the geoeffective length. *Bhattarai et al.* [2012] has shown the geoeffective length to be around 1 R_E during purely northward IMF (Table 3.1). During WHI with periods of northward IMF, the CPCP-B0 potential value mostly represents the reduction of viscous potential with E_y.

Figure (5.5) shows the comparison between the CMIT and the Weimer model. The Weimer model [*Weimer*, 2005] has been scaled up by a factor of 1.54 to match the conductivity issue as discussed in section (5.3). The Weimer model was driven with the the same solar wind condition used for CMIT run. We see that there is generally a good agreement between the two potentials when the potential is larger (i.e during southward IMF), whereas during the northward IMF there is a considerable

69

disagreement. The Weimer model has a minimum potential floor of about 24kV, which corresponds to the viscous potential. So, the scaled Weimer potential in Figure (5.5) has a floor of about 38 kV, which is what is seen in this figure. This is due to the inability of the Weimer model to describe the high latitude electrodynamics during periods of northward IMF. It is during those periods of northward IMF that the viscous potential goes below the B0 potential value which is not incorporated in Weimer empirical model. This issue extends to several coupling models [e.g., *Kan and Lee*, 1979; *Newell et al.*, 2008; *Borovsky*, 2008] which either assumes a positive reconnection rate or no reconnection during northward IMF, however our results show that this is not correct. So, during northward IMF there is no weak positive reconnection rate and the viscous interaction gets attenuated such that the CPP value goes below the viscous potential value.

5.5   Conclusion

   We performed the LFM simulation for the WHI using the real solar wind data as well as performed a run with zero IMF conditions to determine the viscous contribution during the WHI so that we can analyze the effect of magnetic merging. We determined the reconnection potential during the WHI by subtracting the B0 potential and used this reconnection potential to determine the average geoeffective length during the WHI to be 5 R_E during southward IMF. We further found that the LFM model overpredicts the CPP value due to low ionospheric conductivity when using F10.7=74 SFU so that an appropriate scaling factor is required to determine the realistic value. We determined this scaling factor to be 1.54. The CPP obtained from the Weimer model was multiplied by this scaling factor and was seen to be in agreement with the CPP values obtained from the LFM simulation during periods of southward IMF. Whereas, during northward IMF, the Weimer model was seen to

have a floor of about 38 kV (when scaled by 1.54) whereas LFM showed much lower potential due to the reduction in the viscous potential. A good agreement between the scaled Weimer and LFM values for southward IMF shows that the simulation is modeling the basic physics and dynamics of the magnetosphere-ionosphere system and that a proper modeling of the ionospheric conductivity model in the simulation would lead to much closer agreement to the real data.

We also found that when we subtract the total LFM CPP from the B0 CPP, we get a negative value when the IMF is northward for more than 15 mins. The cycle of northward IMF is seen to reduce viscous potential in the LFM simulation thus producing a negative reconnection potential. This means that the empirical functions that model northward IMF as producing simply weak reconnection not adequately describe the global merging mechanism and require modification.

APPENDIX A

LIST OF DATES CORRESPONDING TO STRONG NORTHWARD IMF

A.1 LIST OF DATES CORRESPONDING TO STRONG NORTHWARD IMF

Table A.1. Table listing events with dominant northward IMF period during 1995.

Year	Day	B_z (nT)	B_y (nT)	Min. Pot (kV)	Min. Pot. Time	Max. Pot (kV)	Max. Pot. Time	Total Pot.	Offset Pot.
1995	093	8.01	3.64	-12.7	15:19:14	1.18	15:24:02	13.88	4.77
1995	093	7.5	2	-6.76	16:56:14	1.32	17:02:14	8.08	-1.99
1995	093	8.62	1.24	-13.05	18:40:22	4.16	18:43:06	17.21	4.84
1995	093	7.25	2.7	-21.11	20:21:38	2.59	20:24:14	23.7	4.43
1995	094	5	1.7	-7.13	13:22:14	4.55	13:24:14	11.68	8.69
1995	094	2.74	1.48	-10.54	20:05:22	5.22	20:07:38	15.76	2.51
1995	095	3.15	2.2	-6.58	14:50:38	4.57	14:57:58	11.15	-6.58
1995	106	4.3	0.5	-11.84	14:19:13	0.02	14:33:37	11.86	3.75
1995	106	4.85	2.35	-9.77	16:05:45	0.44	16:10:21	10.21	3.49
1995	107	7.32	3.2	-22.52	20:55:53	0.33	20:46:45	22.85	2.74
1995	107	7.24	2.37	-23.32	22:37:17	2.42	22:34:41	25.74	6.20
1995	117	4.25	0.2	-20.78	17:10:21	2.26	17:18:17	23.04	13.28
1995	121	7.93	-0.58	-20.12	23:11:23	2.4	23:09:39	22.52	3.12
1995	133	10.8	0.28	-22.79	14:03:04	8.99	13:59:52	31.78	-5.22
1995	149	3.2	-0.2	-20.08	17:29:39	0.57	17:40:43	20.65	-6.79
1995	156	1.65	-0.6	-11.61	17:46:49	1.83	17:54:21	13.44	-5.57
1995	156	2.8	-0.55	-20.09	19:31:33	0.04	19:41:29	20.13	5.73
1995	157	3.14	1.3	-12.81	14:12:16	4.8	14:20:44	17.61	-15.67
1995	174	2.9	-1.5	-15.6	19:13:03	0.02	19:26:11	15.62	0.53
1995	321	2.8	0.6	-11.04	14:15:07	0.76	14:09:07	11.8	5.97
1995	321	3.4	0.4	-7.62	20:58:19	3.72	20:50:55	11.34	0.56
1995	326	5.87	-1.1	-13.00	13:10:41	2.21	13:07:49	15.21	1.08
1995	329	3.92	-0.47	-14.34	12:39:56	1.72	12:42:48	16.06	3.32
1995	330	2.79	-1.4	-9.53	20:46:44	0.77	20.42.20	10.3	-3.34
1995	344	4.05	0.9	-9.69	14:36:07	0	14:50:15	9.69	-0.78

Table A.2. Table listing events with dominant northward IMF period from 1996-2003

Year	Day	B_z (nT)	B_y (nT)	Min. Pot (kV)	Min. Pot. Time	Max. Pot (kV)	Max. Pot. Time	Total Pot.	Offset Pot.
1996	076	1.65	0.6	-15.42	16:12:32	1.17	16:09:12	16.59	-2.16
1996	182	2.7	0.97	-11.24	15:01:32	0.13	15:13:56	11.37	3.43
1996	182	1.61	-0.38	-7.27	18:26:48	2.69	18:29:56	9.96	8.95
1996	225	2.47	0.3	-10.22	18:09:36	0.06	18:15:24	10.28	1.31
1996	249	4.85	-0.23	-9.22	13:18:37	3.32	13:20:29	12.54	7.72
1996	249	3.4	-1.5	-9.37	18:21:29	0.39	18:18:33	9.76	-2.44
1996	264	3.5	1.5	-28.48	18:41:00	4.29	18:50:12	32.77	6.88
1996	316	1.6	0.6	-12.27	14:12:39	0.0	14:22:27	12.27	-3.75
1996	317	2.25	0.6	-11.68	17:21:26	2.3	17:15:10	13.98	-3.49
1996	337	6.64	0.5	-9.15	13:17:15	1.22	13:20:03	10.37	4.2
1996	337	7.5	-4.9	-14.03	14:57:11	0.05	15:00:11	14.08	4.44
1997	101	19.95	-4.45	-17.50	13:12	26.93	13:08	44.43	6.62
1997	101	18.27	-3.6	-19.35	14:47:21	16.62	14:49:41	35.97	13.24
1998	176	10.55	1.15	-16.50	14:57:35	6.91	14:54:59	23.41	-6.07
1998	312	25	-0.95	-15.72	14:10:53	36.19	14:07:05	51.91	-5.16
1999	227	11.35	-0.4	-11.60	20:28:03	11.48	20:31:27	23.08	-6.92
2000	144	17	-2	-42.50	20:33:04	12.06	20:28:00	54.56	-12.24
2000	156	12.14	1.01	-5.74	16:13:17	21.69	16:15:57	27.43	0.05
2000	157	11.45	-2.42	-15.26	21:03:09	8.8	21:05:45	24.06	0.14
2000	192	9.8	-1.46	-38.46	13:41:40	9.37	13:38:28	47.83	-9.9
2000	198	18.29	1.8	-40.62	12:23:58	8.46	12:21:02	49.08	12.68
2000	198	12.75	-2.4	-34.96	14:06:18	17.41	14:03:22	52.37	14.99
2000	277	15.55	-1.58	-8.60	19:50:29	13.36	19:48:35	21.96	-0.08
2001	309	13.17	-3.55	-33.21	13:52:59	2.69	13:50:47	35.9	-9.26
2002	246	9.45	-3.32	-11.71	11:58:32	9.14	11:56:32	20.85	-1.99
2002	246	15.25	3.4	-9.56	13:40:36	17.43	13:37:36	26.99	-0.24
2003	295	11.51	2.3	-26.72	20.15:23	7.23	20:11:15	33.95	-2.42
2003	295	11.74	0.55	-9.75	20:58:59	6.11	21:02:07	15.86	0.32
2003	295	11.24	-0.52	-14.64	21:56:47	18.7	21:53:23	33.34	9.57
2003	295	10.71	0.9	-25.62	23:38:07	16.4	23:34:35	42.02	-2.23
2003	342	12.9	1.1	-24.98	13:32:22	33.45	13:27:58	58.43	6.96

APPENDIX B

DATA ANALYSIS PROCEDURE FOR DMSP SATELLITE

In this appendix, we will discuss in detail about the DMSP satellite and the methods used to obtain data used to create figure 3.5.

B.1 DATA ANALYSIS PROCEDURE FOR DMSP SATELLITE

The Defense Meteorological Satellite Program (DMSP) has polar orbiting satellites at an altitude of about 840km and are used primarily for monitoring the meteorological, oceanographic and solar wind-geomagnetic field interaction for the United States Department of Defense. The first DMSP spacecraft was launched January 19, 1965 and there are at least two satellites active at a given time. Starting with DMSP-F8 launched on 1987, the DMSP satellites carry Special Sensors-Ions, Electrons, and Scintillation (SSIES) thermal plasma analysis package built by University of Texas at Dallas to study the IMF-geomagnetic field interaction. For our research propose we used DMSP-F13 satellite. This satellite has a dawn-dusk orbit with a period of about 102 minutes at the max/min altitude of 856/844 km respectively.
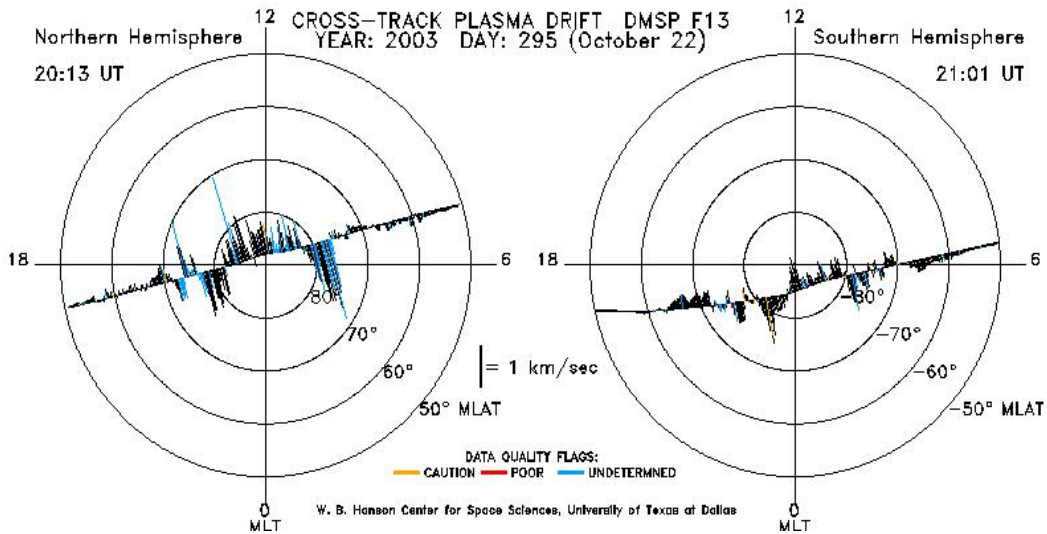

Figure B.1. Diagram showing a pass of the DMSP satellite through both hemispheres. The satellite goes dusk to dawn in the northern and dawn to dusk in the southern hemisphere. Each circle represents a magnetic latitude of 10^0.
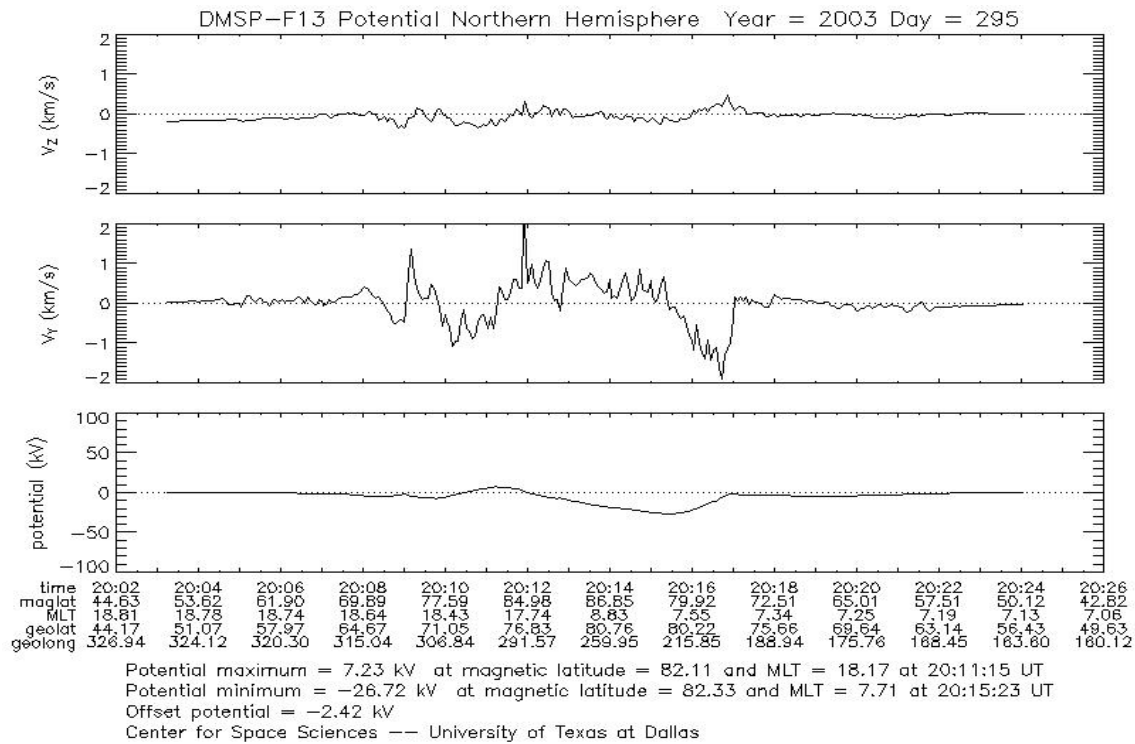
Figure B.2. Diagram showing the variation of Z- and Y- component of drift velocity and potential in the ionosphere as seen by DMSP satellite.

Figure B.1 plots data obtained from DMSP satellite during its fly-over in the northern and the southern hemisphere during period with northward IMF. The two adjacent circles are at a difference of 10^0 magnetic latitude. The black,blue, yellow and red colored histogram shown in the satellite pass represents good, undetermined, caution and poor flag respectively. The Sun is at the top of the page with dawn on the right side of the page. This figure shows that the satellite entered from the night and dusk side of the northern hemisphere, crossed the pole within 80^0 magnetic latitude and exited on the dayside dawn.

The dates to obtain the DMSP satellite plot and data as shown in figure B.1 and B.2 were chosen such that the solar wind was pointing northward for at least 90 min and B_z was at least 1.5 times B_y. The solar wind data was obtained from

77

the CDA web, a website maintained by NASA, that allows us to download all public satellite data.

Figure B.2 shows a plot of data obtained from DMSP satellite during the pass shown in figure B.1. The upper and the middle panel shows the Z- and Y- component of particle drift velocity and the lower panel shows the potential measured. The X-axis has time, the magnetic latitude, the magnetic local time, geographic latitude and geographic longitude axis. The last panel, which plots the potential with respect to universal time, shows a four cell pattern in the ionosphere. From this figure we can measure the CPP by subtracting the maximum and minimum potential. The offset potential value seen in this figure represents the uncertainty in measuring potential. If the offset potential is above 20 percent of the CPP, the data is considered non-usable.

The central panel in the figure shows variation of Y-component of drift velocity during the satellite pass. A positive V_Y along higher latitude implies a sunward flow of the plasma, which is a characteristics of northward IMF as discussed in section 3.2. Also, from this figure we can conclude that it was a reconnection dominated event, i.e. periods when the reconnection potential was greater than the viscous potential.

REFERENCES

Axford, W. I., and C. O. Hines (1961), A unifying theory of high-latitude geophysical phenomena and geomagnetic storms, *Can. J. Phys.*, *39*.

Bhattarai, S. K., and R. E. Lopez (2013), Reduction of viscous potential for northward interplanetary magnetic field as seen in LFM simulation, under Review.

Bhattarai, S. K., R. E. Lopez, R. Bruntz, J. G. Lyon, and M. Wiltberger (2012), Simulation of the polar cap potential during periods with northward interplanetary magnetic field, *J. Geophys. Res.*, *117(A04219)*, doi:10.1029/2011JA017143.

Bochsler, P. (2000), Abundances and charge state of particles in the solar wind, *Rev. Geophys.*, *38*(2), 247–266.

Boris, J. P. (1970), A physically motivated solution of the alfven problem, *Tech. rep.*, Naval Research Laboratory, Washington, D. C., technical Report 2167, NRL memorandum report.

Borovsky, J. E. (2008), The rudiments of a theory of solar wind/magnetosphere coupling derived from first principles, *J. Geophys. Res.*, *113*, A08,228, doi:10.1029/2007JA012646.

Boyle, C., P. Reiff, and M. Hairston (1997), Empirical polar cap potentials, *J. Geophys. Res.*, *102(A1)*, 111125, doi:10.1029/1999JA900031.

Broussard, R. M., R. Tousey, J. H. Underwood, and N. R. Sheeley, Jr. (1978), A survey of coronal holes and their solar wind associations throughout sunspot cycle 20, *Solar Physics*, *56*, 161–183, doi:10.1007/BF00152641.

Bruntz, R., R. E. Lopez, M. Wiltberger, and J. G. Lyon (2012a), Investigation of the viscous potential using an MHD simulation, *J. Geophys. Res.*, *117(A03214)*, 12,975–13,010, doi:10.1029/2011JA017022.

Bruntz, R., R. E. Lopez, S. K. Bhattarai, K. H. Pham, Y. Deng, Y. Huang, M. Wiltberger, and J. G. Lyon (2012b), Investigating the viscous interaction and its role in generating the ionospheric potential during the whole heliosphere interval, *J. Atmos. Sol. Terr. Phys.*, *83*, 70–78, http://dx.doi.org/10.1016/j.jastp.2012.03.016.

Burgess, D. (1995), *Collisionless shocks , in Introduction to Space Physics, edited by M. G. Kivelson and C. T. Russel, pp91-128*, Cambridge University Press.

Burke, W. J., M. C. Kelley, R. C. Sagalyn, M. Smiddy, and S. T. Lai (1979), Polar cap electric field structures with a northward interplanetary magnetic field, *Geophys. Res. Lett.*, *6*, 21–24.

Burke, W. J., D. R. Weimer, and N. C. Maynard (1999), Geoeffective interplanetary scale sizes derived from regression analysis of polar cap potentials, *J. Geophys. Res.*, *104(A5)*, 9989–9994, doi:10.1029/1999JA900031.

Chen, F. F. (1974), *Introduction, in Introduction to Plasma Physics, pp11*, Plenum Press.

Claudepierre, S. G., S. R. Elkington, and M. Wiltberger (2008), Reverse convection, *J. Geophys. Res.*, *113(A05218)*, doi:10.1029/92JA01532.

Courant, R., K. Friedrichs, and H. Lewy (1928), Über die partiellen differentialgleichungen der mathematischen physik, *Math. Ann.*, *100*, 32–74, see translation, On the partial differential equations of mathematical physics, IBM J. Res. Develop. 2 (1967).

Crooker, N. U. (1992), Solar wind driving of magnetospheric ulf waves: Pulsations driven by velocity shear at the magnetopause, *J. Geophys. Res., 97(A12)*, 19,369–19,372, doi:10.1029/2007JA012890.

Cumnock, J. A., R. A. Heelis, M. R. Hairston, and P. T. Newell (1995), High-latitude ionospheric convection pattern during steady northward interplanetary magnetic field, *J. Geophys. Res., 100(A8)*, 14,53714,555, doi:10.1029/94JA03318.

Doyle, M. A., and W. J. Burke (1983), S3-2 measurements of the polar cap potential, *J. Geophys. Res., 88(A11)*, 9125–9133, doi:10.1029/JA088iA11p09125.

Dungey, J. W. (1961), Interplanetary magnetic field and the auroral zones, *Phys. Rev. Lett., 6*, 47–48, doi:10.1103/PhysRevLett.6.47.

Fedder, J., S. Slinker, J. Lyon, and R. Elphinstone (1995), Global numerical simulation of the growth phase and the expansion onset for a substorm observed by viking, *J. Geophys. Res., 100*, 19,083–19,093, doi:10.1029/95JA01524.

Hairston, M. R., T. W. Hill, and R. A. Heelis (2003), Observed saturation of the ionosphere polar cap potential during the 31 march 2001 storm, *J. Geophys. Res, 99*, 5771–5792, doi: 10.1029/2002GL015894.

Hill, T. W., A. J. Dessler, and R. A. Wolf (1976), Mercury and Mars: The role of ionospheric conductivity in the acceleration of magnetospheric particles, *Geophys. Tes. Lett., 3(8)*, 429–432, doi:10.1029/GL003i008p00429.

Huang, C.-S., D. Andre, G. Sofko, and A. Koustov (2000), Observations of Ionospheric Multi-Cell Convection During Northward Interplanetary Magnetic Field, *J. Geophys. Res., 105*, 7419–7428.

Hundhausen, A. J. (1995), *The solar wind , in Introduction to Space Physics, edited by M. G. Kivelson and C. T. Russel, pp91-128*, Cambridge University Press.

Kan, J. R., and L. C. Lee (1979), Energy coupling and the solar wind dynamo, *Geophysical Research Lett.*, *6*, 577, doi:10.1029/GL006i007p00577.

Kivelson, M. G., and A. J. Ridley (2008), Saturation of the polar cap potential: Inference from Alfvén wing arguments, *J. Geophys. Res.*, *113*, A05,214.

Kivelson, M. G., and C. T. Russel (1995), *Introduction to Space Physics*, Cambridge University Press.

Li, W., J. Raeder, J. Dorelli, M. Oieroset, and T. D. Phan (2005), Plasma sheet formation during long period of Northward IMF, *Geophys. Res. Lett.*, *32*, doi:10.1029/2004GL021524.

Liemohn, M. W., J. U. Kozyra, M. R. Hairston, D. M. Weimer, G. Lu, A. J. Ridley, T. H. Zurbuchen, and R. M. Skoug (2002), Consequences of a saturated convection electric field on the ring current, *Geophys. Res. Lett.*, *29(9)*, 1348, doi:10.1029/2001GL014270.

Lopez, R. E., M. Wiltberger, J. G. Lyon, C. C. Goodrich, and K. Papadopoulos (1999), MHD simulations of the response of high-latitude potential patterns and polar cap boundaries to sudden southward turnings of the interplanetary magnetic field, *Geophys. Res. Lett.*, *26(7)*, 967–970, http://dx.doi.org/10.1029/1999GL900113.

Lopez, R. E., S. Hernandez, M. Wiltberger, C.-L. Huang, E. L. Kepko, H. Spence, C. C. Goodrich, and J. G. Lyon (2007), Predicting magnetopause crossings at

geosynchronous orbit during the Halloween storms, *Space Weather*, *5*, S01,005, doi:10.1029/2006SW000222.

Lopez, R. E., J. G. Lyon, E. Mitchell, R. Bruntz, V. G. Merkin, S. Brogl, F. Toffoletto, and M. Wiltberger (2009), Why doesnt the ring current injection rate saturate?, *J. geophys. Res.*, *114*, A02,204, doi:10.1029/ 2008JA013141.

Lopez, R. E., R. Bruntz, E. J. Mitchell, M. Wiltberger, J. G. Lyon, and V. G. Merkin (2010), Role of magnetosheath force balance in regulating the dayside reconnection potential, *J. geophys. Res.*, *115*, A2216, doi:10.1029/2009JA014597.

Lopez, R. E., S. K. Bhattarai, R. Bruntz, K. Pham, M. Wiltberger, J. Lyon, Y. Deng, and Y. Huang (2012), The role of dayside merging in generating the ionospheric potential during the whole heliospheric interval, *J. Atmos. Sol. Terr. Phys.*, *83*, 63–69, doi:10.1016/j.jastp.2012.03.001.

Lyon, J., J. Fedder, and C. Mobarry (2004), The Lyon–Fedder–Mobarry (LFM) global MHD magnetospheric simulation code, *J. Atmos. Sol. Terr. Phys.*, *66*, 1333–1350, doi:10.1016/j.jastp.2004.03.020.

Lyon, J. G., R. E. Lopez, C. C. Goodrich, M. Wiltberger, and K. Papadopoulos (1998), Simulation of the March 9,1995 substorm: Auroral brightening and the onset of lobe reconnection, *Geophys. Res. Lett.*, *25(15)*, 3039–3042.

Mekin, V. G., J. G. Lyon, B. J. Anderson, H. Korth, C. C. Goodrich, and K. Papadopoulos (2007), A global MHD simulation of an event with a quasi-steady northward IMF component, *Ann. Geophys.*, *25*, 1345–1358.

Merkin, K., V., Papadopoulos, G. Milikh, A. S. Sharma, X. Shao, J. Lyon, and C. Goodrich (2003), Effects of the solar wind electric field and ionospheric conduc-

tance on the cross polar cap potential: Results of global MHD modeling, *Geophys. Tes. Lett., 30(23)*, 2180, doi: 10.1029/2003GL017903.

Mitchell, E. J., R. E. Lopez, R. J. Bruntz, M. Wiltberger, J. G. Lyon, R. C. Allen, S. J. Cockrell, and P. L. Whittlesey (2010), Saturation of transpolar potential for large y component interplanetary magnetic field, *J. Geophys. Res., 115(A6)*, A06,201, doi:10.1029/2009JA015119.

Newell, P. T., T. Sotirelis, K. Liou, and F. J. Rich (2008), Pairs of solar wind-magnetosphere coupling functions: Combining a merging term with a viscous term works best, *J. Geophys. Res., 113*, A04,218, doi:10.1029/2007JA012825.

Ober, N. C. M., D. M., and W. J. Burke (2003), Testing the Hill model of transpolar potential saturation, *J. Geophys. Res., 108(A12)*, 1467, doi: 10.1029/2003JA0110154.

Otto, A., and D. Fairfield (2000), Kelvin-Helmholtz instability at the magnetotail boundary: MHD simulation and comparison with Geotail observations, *J. Geophys. Res., 105(A9)*, doi:10.1029/1999JA00031.

Philips, K. J. H. (1995), *Guide to the sun*, Cambridge University Press.

Powell, K. G., P. L. Roe, T. J. Linde, T. I. Gambosi, and D. L. de Zeeuw (1999), A solution-adaptive upwind scheme for ideal magnetohydrodynamics, *Journal of computational physics, 154*, 284–309.

Raeder, J., Y. L. Wang, T. J. Fuller-Rowell, and H. J. Singer (2001), Global simulation of space weather effects on the bastille day storm, *Sol. Phys., 204*, 323–337, doi: 10.1023/A:1014228230714.

Reiff, P., R. Sipro, and T. Hill (1981), Dependence of polar cap potential drop on interplanetary parameters, *J. Geophys. Res.*, *86(A9)*, 7639–7648, doi:10.1029/JA086iA09p07639.

Rich, F. G., and M. Hairston (1994), Large-scale convection patterns observed by DMSP, *J. Geophys. Res.*, *99(A3)*, 3827–3844.

Richmond, A. D., E. C. Ridley, and R. G. Roble (1992), A thermosphere/ionosphere general circulation model with coupled electrodynamics, *Geophys. Res. Lett.*, *19*(6), 601–604, doi:10.1029/92GL00401.

Ridley, A. J. (2007), Alfveń wings at Earths magnetosphere under strong interplanetary magnetic field, *Ann. Geophys*, *25*, 533–542.

Russell, C. T., J. G. Luhmann, and G. Lu (2001), Nonlinear response of the polar ionosphere to large values of the interplanetary electric field, *J. Geophys. Res.*, *106*, 18,495–18,504, doi:10.1029/2001JA900053.

Shepherd, S. G., R. A. Greenwald, and J. M. Ruohoniemi (2002), Cross polar cap potentials measured with super auroral radar network during quasi-steady solar wind and interplanetary magnetic field conditions, *J. Geophys. Res.*, *107(A7)*, doi:10.1029/2001JA000152.

Shepherd, S. G., J. M. Ruohoniemi, and R. A. Greenwald (2003), Testing the hill model of transpolar potential with Super Dual Auroral Radar Network observations, *Geophys. Res. Lett.*, *30(1)*, doi:10.1029/2002GL015426.

Siscoe, G. L., G. M. Erickson, a. N. C. M. B. U. O. Sonnerup, J. A. Schoendorf, K. D. Siebert, D. R. Weimer, W. W. White, and G. R. Wilson (2002a), Hill model

of transpolar potential saturation: Comparison with MHD simulation, *J. Geophys. Res., 107(A6)*, 10.1029/2001JA000109.

Siscoe, G. L., N. U. Crooker, and K. D. Siebert (2002b), Transpolar potential saturation: Roles of region 1 current system and solar wind ram pressure, *J. Geophys. Res., 107(A10)*, doi:10.1029/2001JA009176.

Song, P., T. I. Gombosi, D. L. DeZeeuw, K. G. Powell, and C. P. T. Groth (2000), A model of solar wind-magnetosphere-ionosphere coupling for due northward IMF, *Planetary and Space Science, 48*(1), 29 – 39, doi:10.1016/S0032-0633(99)00065-3.

Sonnerup, B., K. Siebert, W. White, D. Weimer, N. Maynard, J. Schoendorf, G. Wilson, G. Siscoe, and G. Erickson (2001), Simulations of the magnetosphere for zero interplanetary magnetic field: The ground state, *J. Geophys. Res., 106(A12)*, 29,41929,434, 10.1029/2001JA000124.

Sundberg, K. A. T., J. A. Cumnock, and L. G. Bloomberg (2009a), Reverse convection potential: A statistical study of the general properties of lobe reconnection and saturation effects during northward IMF, *J. Geophys. Res., 114*, A06,205, 10.1029/2008JA013838.

Sundberg, K. A. T., L. G. Bloomberg, and J. A. Cumnock (2009b), Properties of the boundary layer potential for northward interplanetary magnetic field, *Geophys. Res. Lett., 36*, L11,104, 10.1029/2009GL038625.

Walker, R. J., and C. T. Russell (1995), *Solar wind interactions with magnetized planets, in Introduction to Space Physics, edited by M. G. Kivelson and C. T. Russell, pp 169*, Cambridge University Press, New York, NY.

Weimer, D. R. (2005), Improved ionospheric electrodynamic models and application to calculating Joule heating rates, *J. Geophys. Res.*, *110*, A05,306, doi:10.1029/2004JA010884.

Wilder, F. D., C. R. Clauer, and J. B. H. Baker (2008), Reverse convection potential saturation during northward IMF, *Geophys. Res. Lett.*, *35*, L12,103, doi:10.1029/2008GL034040.

Wilder, F. D., C. R. Clauer, and J. B. H. Baker (2009), Reverse convection potential saturation during northward IMF under various driving conditions, *J. Geophys. Res.*, *114*, A08,209, doi:10.1029/2009JA014266.

Wilder, F. D., C. R. Clauer, and J. B. H. Baker (2010), Polar cap electric field saturation during interplanetary magnetic field Bz north and south conditions, *J. Geophys. Res.*, *115*, A10,230, doi:10.1029/2010JA015487.

Wiltberger, M., T. S. Weigel, M. Gehmeyr, and T. Guild (2005), Analysis and visualization of space science model output and data with CISM-DX, *J. Geophys. Res.*, *110*, A09,224, doi:10.1029/2004JA010956.

Wygant, J. R., R. B. Torbert, and F. S. Mozer (1983), Comparisonof S3-3 polar cap potential drops with the interplanetary magnetic field and models of magnetopause reconnection, *J. Geophys. Res.*, *88(A7)*, 5727–5735, doi:10.1029:/JA088iA07p05727.

BIOGRAPHICAL STATEMENT

Shree K. Bhattarai was born in Kathmandu, Nepal, in 1980 A.D. He received his B.Sc from Amrit Science Campus, Kathmandu, Nepal, in 2002 A.D; his M.Sc degree in Physics from Department of Physics, Tribhuwan University, kathmandu, Nepal in 2006 A.D., and his Ph.D degree in physics from the University of Texas at Arlington in 2013 A.D. He worked as a Lecturer of Physics in Reliance College, Orient College and BST College, at Kathmandu, Nepal from 2006-2008 A.D. His current research interest is in the area of prediction of impact of change in Space weather to the human society. He is a member of American Physical Society(APS) and American Geophysical Society(AGU) and was the founder secretary of Social Welfare Sports Center, a Sports based club in Nepal dedicated to involving children in sport activities.